

# Decoupling of temperature and pH gradients along the equatorial Pacific during the Pliocene

Pincelli Hull (✉ [pincelli.hull@yale.edu](mailto:pincelli.hull@yale.edu))

Yale University

**Madison Shankle**

University of St Andrews <https://orcid.org/0000-0002-8052-9136>

**Natalie Burls**

George Mason University <https://orcid.org/0000-0002-6950-3808>

**Alexey Fedorov**

Yale University

**Matthew Thomas**

University Corporation for Atmospheric Research/GFDL

**Donald Penman**

Utah State University

**Heather Ford**

Queen Mary University of London <https://orcid.org/0000-0002-8081-7023>

**Peter Jacobs**

George Mason University

**Noah Planavsky**

Yale University

---

## Physical Sciences - Article

**Keywords:** Equatorial Pacific Dynamics, Tropical Climate Patterns, Global Warming, Wind-driven Upwelling, Meridional Overturning Cell, Thermal Stratification

**Posted Date:** December 10th, 2020

**DOI:** <https://doi.org/10.21203/rs.3.rs-118082/v1>

**License:** © ⓘ This work is licensed under a Creative Commons Attribution 4.0 International License.

[Read Full License](#)

---

**Version of Record:** A version of this preprint was published at Nature on October 20th, 2021. See the published version at <https://doi.org/10.1038/s41586-021-03884-7>.



# **Decoupling of temperature and pH gradients along the equatorial Pacific during the Pliocene**

**Authors:** Madison G. Shankle<sup>1, †\*</sup>, Natalie J. Burls<sup>2</sup>, Alexey V. Fedorov<sup>1</sup>, Matthew D. Thomas<sup>3</sup>, Donald E. Penman<sup>1, ††</sup>, Heather L. Ford<sup>4</sup>, Peter Jacobs<sup>5</sup>, Noah J. Planavsky<sup>1</sup>, Pincelli M. Hull<sup>1\*</sup>

## **Affiliations:**

5   <sup>1</sup>Department of Earth and Planetary Sciences, Yale University, New Haven, CT, 06511, USA.

<sup>2</sup>Department of Atmospheric, Oceanic & Earth Sciences, George Mason University, Fairfax, VA, 22030, USA.

<sup>3</sup>University Corporation for Atmospheric Research/GFDL, Princeton, NJ, 08540, USA.

<sup>4</sup>School of Geography, Queen Mary University of London, London, E1 4NS, UK.

10   <sup>5</sup>Department of Environmental Science and Policy, George Mason University, Fairfax, VA, 22030, USA.

     \*Correspondence to: [mgs23@st-andrews.ac.uk](mailto:mgs23@st-andrews.ac.uk), [pincelli.hull@yale.edu](mailto:pincelli.hull@yale.edu).

     †Current address: School of Earth & Environmental Sciences, University of St Andrews, St Andrews, KY16 9AL, UK.

15   ††Current address: Department of Geosciences, Utah State University, Logan, UT, 94321 USA.

### Summary Paragraph:

25           Equatorial Pacific dynamics drive tropical climate patterns such as the El Niño-Southern  
Oscillation and provide nutrients for one of the world's most productive marine ecosystems. How  
this region will respond to global warming remains an important area of study with profound  
implications for both human wellbeing and economic and ecosystem stability. In light of this,  
numerous studies have investigated equatorial Pacific dynamics during the Pliocene epoch (5.3-  
30   2.6 million years ago) as an analogue for future behavior of the region under global warming<sup>1-12</sup>.  
Current paleoceanographic records from the Pliocene tropical Pacific present an apparent paradox,  
with proxy evidence of a reduced east-west sea surface temperature gradient along the  
equator<sup>1,5,6,11</sup>— indicative of reduced wind-driven upwelling — conflicting with evidence of  
enhanced biological productivity in the region<sup>13-15</sup> which is typically driven by upwelling. Here  
35   we reconcile these observations by providing new evidence for older, more acidic, and nutrient-  
rich water reaching the equatorial Pacific by way of a Pacific meridional overturning cell during  
the Pliocene<sup>16</sup>. This provides a mechanism by which enhanced productivity could have existed  
alongside a reduced east-west sea surface temperature gradient in the Pliocene equatorial Pacific.  
Furthermore, these results challenge the current paradigm of a decline in biological productivity  
40   in warmer worlds due to enhanced thermal stratification<sup>17</sup>. Our findings shed a new light on  
equatorial Pacific dynamics and help constrain potential changes to them in the near-future, given  
that the Earth is expected to reach Pliocene-like temperatures by the end of the century. The  
equatorial Pacific is a region of great significance as it hosts one of the most important climate  
phenomena on the planet, the El Niño Southern Oscillation<sup>18</sup>, and supports massively productive  
45   fisheries that provide key ecosystem services to numerous communities<sup>19,20</sup>, and our results  
provide novel insight on how it might change as the oceans adjust to a warming world.

## Main Text:

A salient feature of the modern tropical Pacific climate is a pronounced zonal (east-west) sea surface temperature (SST) gradient along the equator with mean temperature decreasing from ~29°C in the western Pacific warm pool to ~23°C in the eastern Pacific equatorial cold tongue<sup>2</sup>. This zonal SST gradient is tightly coupled to the Pacific zonal atmospheric circulation—known as the Walker cell—whose winds in turn control the zonal tilt of the oceanic thermocline and the strength of equatorial upwelling via the Bjerknes feedback<sup>21</sup>. The Pacific zonal SST gradient thus plays a key role in defining the climate of the tropics. Variations in this gradient produce the El Niño-Southern Oscillation—a dominant mode of interannual climate variability in the tropics and beyond<sup>18</sup>. In addition, vigorous upwelling in the eastern tropical Pacific brings low-pH, nutrient-rich water up into the surface ocean, supporting highly productive marine ecosystems important to the economic health and food security of adjacent nations<sup>22,23</sup> and at the same time providing a significant source of carbon dioxide (CO<sub>2</sub>) outgassing during non-El Niño periods<sup>24–26</sup>.

Despite the importance of the Pacific zonal SST gradient for climate and marine ecosystems, considerable uncertainty persists in how this ocean feature will respond to global warming<sup>27</sup>. One approach is to turn to past warm climates like the Pliocene epoch—the last time in Earth’s history when atmospheric CO<sub>2</sub> concentrations were similar (300-450ppm) to the anthropogenically-forced levels seen today<sup>8,28</sup>—in order to develop a better understanding of tropical Pacific dynamics during near-equilibrium warmer climate states.

Existing records of Pliocene equatorial Pacific environments and biogeochemical cycling present a paradox. Today, a decrease in the zonal temperature gradient corresponds to reduced biological productivity in the eastern equatorial Pacific due to reduced upwelling of nutrient-rich waters, such as occurs during a modern-day El Niño event. Perplexingly, Pliocene records seem

70 to show a decoupling between the zonal SST gradient and biological productivity. Multiple studies suggest that the Pliocene climate was characterized by a reduced zonal temperature gradient and a deeper/warmer thermocline relative to modern<sup>1,2,4,7,8,11,12</sup>—suggestive of a “permanent El Niño”-like background state or “El Padre”<sup>1,3,10</sup>. While debates continue on the magnitude of this gradient reduction<sup>4,9–11</sup>, a broad agreement exists that the Pliocene east-west equatorial SST gradient was  
75 indeed substantially weaker. However, despite the reduced zonal SST gradient and therefore the presumed weaker atmospheric Walker circulation and wind-driven upwelling, the eastern equatorial Pacific (EEP) was highly productive during this time<sup>13–15</sup>.

One solution to this paradox would be for the upwelled Pliocene water to have been extremely nutrient-rich, such that a smaller volume of upwelled water would support greater  
80 productivity, but whether and why this might occur has been unclear. Deep water that is upwelled to the surface contains more nutrients than surface water due to the remineralization of organic matter which liberates nutrients along with CO<sub>2</sub>, resulting in a decrease in the upwelled water’s pH. The acidity and nutrient content of the upwelled water also varies based on the age of the upwelled water, with the upwelling of older water masses contributing more acidity and nutrients  
85 to the surface than a similar volume of relatively younger water. Thus, the upwelling of deeper and/or older water in the EEP during the Pliocene could account for the productivity seen there in the face of weaker overall upwelling. While it is difficult to reconstruct nutrient delivery in upwelling areas, the boron isotopic ( $\delta^{11}\text{B}$ ) composition of planktonic foraminifera provides a robust pH proxy for tracing changes in the chemical composition of seawater through time<sup>29,30</sup>.  
90 Here we use that proxy to reconstruct the Pacific zonal pH gradient along the equator to test this potential solution to the Pliocene paradox. Critically, different paradigms of Pliocene climate states, in which physical (SST) and biogeochemical (pH) gradients are either coupled or not, make

distinct predictions about east and west tropical Pacific pH values and gradients (Fig. 1). Because surface pH values are strongly linked to regional and basin-scale ocean circulation patterns, which  
95 of these states the Pliocene Pacific operated under has major implications for atmospheric circulation, weather patterns, and ocean productivity. The boron-pH proxy therefore offers a potent tool for constraining both Pliocene tropical climate and ocean dynamics.

The  $\delta^{11}\text{B}$ -pH proxy is based on the pH-dependent speciation of boron between two predominant aqueous species in seawater: boric acid ( $\text{B}(\text{OH})_3$ ) at low pH and borate ion ( $\text{B}(\text{OH})_4^-$ )  
100 ) at high pH, with an equilibrium fractionation of  $\text{B}^{10}$  and  $\text{B}^{11}$  between these two species. Only borate ion is believed to be incorporated into biogenic carbonates and thus there is a predictable relationship between the  $\delta^{11}\text{B}$  of biogenic calcite (specifically, of planktonic foraminifera for the surface ocean) and ambient ocean pH<sup>29,30</sup>. Using boron isotopes, we thus reconstruct zonal pH gradients in the tropical Pliocene Pacific (Fig. 2) and use global circulation models to provide a  
105 mechanistic explanation for the apparent Pliocene paradox.

Here we analyzed  $\delta^{11}\text{B}$  in ~100-shells per sample of the near surface-dwelling foraminifer *Orbulina universa* from the western equatorial Pacific (WEP, ODP Site 806) and eastern equatorial Pacific (EEP, ODP Site 846) at ~1Ma, ~3Ma, and ~6Ma. Each time slice includes four samples spanning ~300kyr. Our data are largely coherent at a given site within any given time slice. In the  
110 WEP,  $\delta^{11}\text{B}$  averaged 17.67 (1Ma), 16.63 (3Ma), and 16.76 (6Ma) ‰ (mean analytical uncertainty [ $2\sigma$ ] = 0.24‰), indicating a decrease in pH from a preindustrial value<sup>31</sup> of ~8.10 to ~8.02 in the late Miocene/early Pliocene (~6 Ma, mean pH uncertainty [ $2\sigma$ ] ~0.05 from Monte Carlo simulations) (Fig. 2). Our surface pH estimates for the WEP—a region understood to be approximately in equilibrium with the atmosphere<sup>25</sup>—are consistent with the decline one would  
115 expect in response to current estimates of atmospheric  $\text{CO}_2$  concentrations during each interval.

Our pH values give atmospheric  $p\text{CO}_2$  estimates of  $331 \pm 48$  ppm [ $2\sigma$ ] at 1Ma,  $434 \pm 64$  ppm at 3Ma,  $439 \pm 64$  ppm at 6Ma when assuming a generous range around the approximate modern-day value for alkalinity ( $2275 \pm 200$   $\mu\text{mol/kg}^{32}$ ) (Fig. S1). Alkalinity is understood to have remained relatively invariant over the Cenozoic<sup>33</sup>, making it a robust assumption to use, however the  
120 assumption of a modern-like value for the calcite saturation state with a generous range ( $\Omega = 5 \pm 2$ ) gives similar results (Fig. S2).

In the EEP (ODP Site 846), pH likewise declines from ~1 to ~6 Ma but at a magnitude larger than the west, declining from a preindustrial  $\text{pH}^{31}$  value of ~8.05 to ~7.88 at ~6Ma (uncertainty [ $2\sigma$ ] ~0.06) (Fig. 2). This results in much greater zonal pH gradients (~3-4 times  
125 greater) at ~3-6Ma than in the preindustrial ocean (preindustrial  $\text{pH}^{31}$  gradient ~0.05). The average zonal pH gradient (Fig. 2) varies from 0.04 to ~0.17 to ~0.14 at ~1Ma, ~3Ma, and ~6Ma, respectively.

This three-fold increase in the Pliocene equatorial Pacific zonal pH gradient is inconsistent with an El Niño-like coupling of physical (SST) and biogeochemical (pH) gradients (Fig. 1, coupled scenarios). Rather, our reconstructed zonal pH gradient suggests changes in zonal SST  
130 and pH gradients were decoupled in the Pliocene (Fig. 1, decoupled). New simulations using a coupled ocean-atmosphere climate model with active biogeochemical cycles (the Community Earth System Model, CESM 1.0.4, see Methods), which reproduces large-scale surface temperature gradients resembling Pliocene SST reconstructions<sup>16,34,35</sup>, generate pH changes  
135 similar to our results (Fig. 3). The modeled Pliocene ocean has pH values of ~8.00-8.05 in the WEP and ~7.80-7.85 in the EEP (Fig. 3a) at 55m depth (the approximate habitat of *O. universa*<sup>36-38</sup>), similar to our  $\delta^{11}\text{B}$ -pH proxy data. Model output over 25-75m depth generally agrees with  $\delta^{11}\text{B}$ -pH proxy data, however (Figs. S3, S4). This proxy-model agreement provides compelling



evidence for increased zonal pH gradients in the Pliocene even as zonal temperature gradients were  
140 decreased<sup>1,5,6,9,11</sup> (Figs. 2, 3; Figs. S4, S5).

The Pliocene model simulations suggest that the enhanced ocean acidity in the east relative  
to the west can be explained by a large-scale reorganization of Pacific circulation associated with  
deep water formation in the North Pacific and an active Pacific meridional overturning circulation  
(PMOC)<sup>16</sup>, both of which are absent in the Pacific Ocean today. The modeled Pliocene PMOC  
145 strength is ~17 Sverdrups ( $1 \text{ Sv} = 10^6 \text{ m}^3 \text{ s}^{-1}$ ), comparable to the modern Atlantic meridional  
overturning circulation (AMOC). Several features of the Pliocene PMOC contribute to the  
anomalously acidic water in the EEP cold tongue. First, deep water formation in the North Pacific  
introduces an anomalous interhemispheric gradient in mid- to deep water pH relative to the  
preindustrial ocean, with high-pH water in the Northern Hemisphere and low-pH water in the  
150 Southern Hemisphere (at the end of PMOC and AMOC flow paths (Fig. 4a)). Second, PMOC  
brings deeper, low-pH water to intermediate depths (1000 m) (Fig. 4b). This acidic intermediate  
water is then readily upwelled in the EEP because of a warm, less stratified thermocline relative  
to modern<sup>3,7</sup>. A Lagrangian analysis of the trajectories of water parcels subducted during North  
Pacific deep-water formation (Fig. 4c) confirms that about 10% of this water is upwelled in the  
155 EEP. On average, these water parcels take ~800 years to arrive at the equator, while some parcels  
may take several millennia, which contributes to their low pH due to the accumulation of respired  
organic carbon as they circulate. In the modern climate, EEP thermocline waters originate in  
subtropical cells and only take ~10-60 years after subduction to transit into the EEP<sup>39</sup>.

The upwelling of old, acidic water in the east Pacific and presumed delivery of more  
160 nutrients to the surface ocean contrasts with the conventional view that nutrient delivery and  
productivity in warm oceans will be low, particularly in the eastern tropical Pacific, due to

decreased wind-driven upwelling<sup>17</sup>. Our coupled boron isotope data and model results show that old, more acidic, intermediate water can upwell in the EEP as a result of PMOC and decreased thermal stratification in the uppermost ocean. Our results provide a dynamic mechanism for the enhanced biological productivity in the east Pacific despite warmer SSTs and a reduced zonal SST gradient during the Pliocene, resolving the apparent paradox of decoupled SSTs and biological productivity.

The implications of our results for the future of the EEP depend on the time scale involved. Modeling results suggest such an El Niño-like mean ocean state may take roughly ~100-200 years to develop in response to a rise in pCO<sub>2</sub> levels<sup>27,40</sup>. However, the long adjustment timescale of the deep ocean circulation implies that it would take on the order of ~1000-1500 years for PMOC to develop in response to this warming (Fig. S4). In other words, the decoupling of temperature and pH gradients is predicted to develop progressively over a period of a thousand years or longer. This warming and stratification in the EEP is still of concern since EEP upwelling currently supports one of the most productive fisheries in the world and provides key economic and ecosystem services to local communities<sup>19,20</sup>. More broadly, our results provide novel constraints on the structure and dynamics of the Pliocene ocean by moving beyond the SST proxies typically employed and help constrain future changes in ocean dynamics and the oceans adjust to a warming world.

## References:

1. Wara, M. W., Ravelo, A. C. & Delaney, M. L. Permanent El Niño-like conditions during the Pliocene warm period. *Science* (80-. ). **309**, 758–761 (2005).
2. Fedorov, A. V *et al.* The Pliocene Paradox (Mechanisms for a Permanent El Niño). *Science* (80-. ). **312**, 1485–1490 (2006).

- 185 3. Ford, H. L., Ravelo, A. C., Dekens, P. S., LaRiviere, J. P. & Wara, M. W. The evolution  
of the equatorial thermocline and the early Pliocene El Padre mean state. *Geophys. Res.  
Lett.* **42**, 4878–4887 (2015).
4. Tierney, J. E., Haywood, A. M., Feng, R., Bhattacharya, T. & Otto-Bliesner, B. L.  
Pliocene warmth consistent with greenhouse gas forcing. *Geophys. Res. Lett.* **46**, 9136–  
190 9144 (2019).
5. Lawrence, K. T., Liu, Z. & Herbert, T. D. Evolution of the eastern tropical Pacific through  
Plio-Pleistocene glaciation. *Science (80-. )*. **312**, 79–83 (2006).
6. Dekens, P. S., Ravelo, A. C. & McCarthy, M. D. Warm upwelling regions in the Pliocene  
warm period. *Paleoceanography* **22**, 1–12 (2007).
- 195 7. Ford, H. L., Ravelo, A. C. & Hovan, S. A deep Eastern Equatorial Pacific thermocline  
during the early Pliocene warm period. *Earth Planet. Sci. Lett.* **355**, 152–161 (2012).
8. Fedorov, A. V *et al.* Patterns and mechanisms of early Pliocene warmth. *Nature* **496**, 43–  
49 (2013).
9. O’Brien, C. L. *et al.* High sea surface temperatures in tropical warm pools during the  
200 Pliocene. *Nat. Geosci.* **7**, 606–611 (2014).
10. Ravelo, A. C., Lawrence, K. T., Fedorov, A. & Ford, H. L. Comment on “A 12-million-  
year temperature history of the tropical Pacific Ocean”. *Science (80-. )*. **346**, 1467 (2014).
11. Zhang, Y. G., Pagani, M. & Liu, Z. A 12-Million-Year Temperature History of the  
Tropical Pacific Ocean. *Science (80-. )*. **344**, 84–88 (2014).
- 205 12. Fedorov, A. V, Burls, N. J., Lawrence, K. T. & Peterson, L. C. Tightly linked zonal and  
meridional sea surface temperature gradients over the past five million years. *Nat. Geosci.*  
**8**, 975–980 (2015).

13. Lyle, M. Neogene carbonate burial in the Pacific Ocean. *Paleoceanography* **18**, (2003).
14. Lyle, M. & Baldauf, J. Biogenic sediment regimes in the Neogene equatorial Pacific,  
210 IODP Site U1338: Burial, production, and diatom community. *Palaeogeogr.*  
*Palaeoclimatol. Palaeoecol.* **433**, 106–128 (2015).
15. Ma, Z., Ravelo, A. C., Liu, Z., Zhou, L. & Paytan, A. Export production fluctuations in  
the eastern equatorial Pacific during the Pliocene-Pleistocene: Reconstruction using barite  
accumulation rates. *Paleoceanography* **30**, 1455–1469 (2015).
- 215 16. Burls, N. J. *et al.* Active Pacific meridional overturning circulation (PMOC) during the  
warm Pliocene. *Sci. Adv.* **3**, e1700156 (2017).
17. Sarmiento, J. L., Hughes, T. M. C., Stouffer, R. J. & Manabe, S. Simulated response of the  
ocean carbon cycle to anthropogenic climate warming. *Nature* **393**, 245–249 (1998).
18. Philander, S. G. El Niño, La Niña, and the southern oscillation. *Int. Geophys. Ser.* **46**, 289  
220 (1989).
19. Christensen, V., De la Puente, S., Sueiro, J. C., Steenbeek, J. & Majluf, P. Valuing  
seafood: The Peruvian fisheries sector. *Mar. Policy* **44**, 302–311 (2014).
20. Gutierrez, D., Akester, M. & Naranjo, L. Productivity and sustainable management of the  
Humboldt Current large marine ecosystem under climate change. *Environ. Dev.* **17**, 126–  
225 144 (2016).
21. Bjerknes, J. Atmospheric teleconnections from the equatorial Pacific. *Mon. Wea. Rev.* **97**,  
163–172 (1969).
22. Iizumi, T. *et al.* Impacts of El Niño Southern Oscillation on the global yields of major  
crops. *Nat. Commun.* **5**, 1–7 (2014).
- 230 23. Anderson, W., Seager, R., Baethgen, W. & Cane, M. Crop production variability in North

and South America forced by life-cycles of the El Niño Southern Oscillation. *Agric. For. Meteorol.* **239**, 151–165 (2017).

24. Feely, R. A. *et al.* Decadal variability of the air-sea CO<sub>2</sub> fluxes in the equatorial Pacific Ocean. *J. Geophys. Res. Ocean.* **111**, (2006).
- 235 25. Takahashi, T. *et al.* Climatological mean and decadal change in surface ocean pCO<sub>2</sub>, and net sea–air CO<sub>2</sub> flux over the global oceans. *Deep Sea Res. Part II Top. Stud. Oceanogr.* **56**, 554–577 (2009).
26. Martínez-Botí, M. A. *et al.* Boron isotope evidence for oceanic carbon dioxide leakage during the last deglaciation. *Nature* **518**, 219–222 (2015).
- 240 27. Heede, U. K., Fedorov, A. V & Burls, N. J. Time Scales and Mechanisms for the Tropical Pacific Response to Global Warming: A Tug of War between the Ocean Thermostat and Weaker Walker. *J. Clim.* **33**, 6101–6118 (2020).
28. Foster, G. L., Royer, D. L. & Lunt, D. J. Future climate forcing potentially without precedent in the last 420 million years. *Nat. Commun.* **8**, 14845 (2017).
- 245 29. Rae, J. W. B., Foster, G. L., Schmidt, D. N. & Elliott, T. Boron isotopes and B/Ca in benthic foraminifera: Proxies for the deep ocean carbonate system. *Earth Planet. Sci. Lett.* **302**, 403–413 (2011).
30. Rae, J. W. B. Boron isotopes in foraminifera: Systematics, biomineralisation, and co<sub>2</sub> reconstruction. in *Boron Isotopes* 107–143 (Springer, 2018).
- 250 31. Feely, R. A., Doney, S. C. & Cooley, S. R. Ocean acidification: Present conditions and future changes in a high-CO<sub>2</sub> world. *Oceanography* **22**, 36–47 (2009).
32. Takahashi, T. *et al.* Climatological distributions of pH, pCO<sub>2</sub>, total CO<sub>2</sub>, alkalinity, and CaCO<sub>3</sub> saturation in the global surface ocean, and temporal changes at selected locations.

*Mar. Chem.* **164**, 95–125 (2014).

- 255 33. Zeebe, R. E. & Tyrrell, T. History of carbonate ion concentration over the last 100 million years II: Revised calculations and new data. *Geochim. Cosmochim. Acta* **257**, 373–392 (2019).
34. Burls, N. J. & Fedorov, A. V. Simulating Pliocene warmth and a permanent El Niño-like state: The role of cloud albedo. *Paleoceanography* **29**, 893–910 (2014).
- 260 35. Burls, N. J. & Fedorov, A. V. What controls the mean east–west sea surface temperature gradient in the equatorial Pacific: The role of cloud albedo. *J. Clim.* **27**, 2757–2778 (2014).
36. Sautter, L. R. & Thunell, R. C. Planktonic foraminiferal response to upwelling and seasonal hydrographic conditions; sediment trap results from San Pedro Basin, Southern California Bight. *J. Foraminifer. Res.* **21**, 347–363 (1991).
- 265 37. Hennehan, M. J. *et al.* A new boron isotope–pH calibration for *Orbulina universa*, with implications for understanding and accounting for ‘vital effects’. *Earth Planet. Sci. Lett.* **454**, 282–292 (2016).
38. Rebotim, A. *et al.* Factors controlling the depth habitat of planktonic foraminifera in the subtropical eastern North Atlantic. *Biogeosciences* **14**, 827–859 (2017).
- 270 39. Thomas, M. D. & Fedorov, A. V. The eastern subtropical Pacific origin of the equatorial cold bias in climate models: A Lagrangian perspective. *J. Clim.* **30**, 5885–5900 (2017).
40. Fedorov, A. V, Brierley, C. M. & Emanuel, K. Tropical cyclones and permanent El Niño in the early Pliocene epoch. *Nature* **463**, 1066–1070 (2010).
- 275 41. Liu, J. *et al.* Eastern equatorial Pacific cold tongue evolution since the late Miocene linked to extratropical climate. *Sci. Adv.* **5**, eaau6060 (2019).

42. Foster, G. L., Pogge von Strandmann, P. A. E. & Rae, J. W. B. Boron and magnesium isotopic composition of seawater. *Geochemistry, Geophys. Geosystems* **11**, (2010).
43. Martínez-Botí, M. A. *et al.* Plio-Pleistocene climate sensitivity evaluated using high-  
280 resolution CO<sub>2</sub> records. *Nature* **518**, 49–54 (2015).
44. Mayer, L. A. *et al.* Proceedings of the Ocean Drilling Program. VOLUME 13 8 INITIAL  
REPORTS PART I EASTERN EQUATORIAL PACIFIC Covering Leg 138 of the cruises  
of the Drilling Vessel JOIDES Resolution, Balboa, Panama, to San Diego, California,  
Sites 844-854, 6 May 1991-5 July 19. (1992).
- 285 45. Kroenke, L. W., Berger, W. H. & others, A. 27. Proceedings of the Ocean Drilling  
Program, Vol. 130, Initial Reports, Ontong Java Plateau. in (Ocean Drilling Program,  
1991).
46. Chaisson, W. P. & Ravelo, A. C. Pliocene development of the east-west hydrographic  
gradient in the equatorial Pacific. *Paleoceanography* **15**, 497–505 (2000).
- 290 47. Ravelo, A. C., Dekens, P. S. & McCarthy, M. Evidence for El Niño-like conditions during  
the Pliocene. *Gsa Today* **16**, 4 (2006).
48. Karnauskas, K. B., Mittelstaedt, E. & Murtugudde, R. Paleooceanography of the eastern  
equatorial Pacific over the past 4 million years and the geologic origins of modern  
Galapagos upwelling. *Earth Planet. Sci. Lett.* **460**, 22–28 (2017).
- 295 49. Lisiecki, L. E. & Raymo, M. E. A Pliocene-Pleistocene stack of 57 globally distributed  
benthic  $\delta^{18}\text{O}$  records. *Paleoceanography* **20**, (2005).
50. Zhang, Y. G., Pagani, M., Henderiks, J. & Ren, H. A long history of equatorial deep-water  
upwelling in the Pacific Ocean. *Earth Planet. Sci. Lett.* **467**, 1–9 (2017).
51. Ogg, J. G., Gradstein, F. M. & Smith, A. G. *A geologic time scale 2004*. **86**, (Cambridge

- 300 University Press, 2004).
52. Spezzaferri, S. *et al.* Fossil and genetic evidence for the polyphyletic nature of the planktonic foraminifera "Globigerinoides", and description of the new genus *Trilobatus*. *PLoS One* **10**, (2015).
53. Foster, G. L. Seawater pH, pCO<sub>2</sub> and [CO<sub>2</sub>– 3] variations in the Caribbean Sea over the last 130 kyr: A boron isotope and B/Ca study of planktic foraminifera. *Earth Planet. Sci. Lett.* **271**, 254–266 (2008).
54. Kiss, E. Ion-exchange separation and spectrophotometric determination of boron in geological materials. *Anal. Chim. Acta* **211**, 243–256 (1988).
55. Okai, T., Suzuki, A., Kawahata, H., Terashima, S. & Imai, N. Preparation of a new Geological Survey of Japan geochemical reference material: Coral JCp-1. *Geostand. Newsl.* **26**, 95–99 (2002).
56. Al-Ammar, A. S., Gupta, R. K. & Barnes, R. M. Elimination of boron memory effect in inductively coupled plasma-mass spectrometry by ammonia gas injection into the spray chamber during analysis. *Spectrochim. Acta Part B At. Spectrosc.* **55**, 629–635 (2000).
- 315 57. Berner, E. K. & Berner, R. A. Global environment water, air, and geochemical cycles Prentice-Hall. *Englewood Cliffs, New Jersey* (1996).
58. Broecker, W. S. & Peng, T. S. Tracers in the Sea Eldigio Press. *Palisades, NY* (1982).
59. Fantle, M. S. & DePaolo, D. J. Sr isotopes and pore fluid chemistry in carbonate sediment of the Ontong Java Plateau: Calcite recrystallization rates and evidence for a rapid rise in seawater Mg over the last 10 million years. *Geochim. Cosmochim. Acta* **70**, 3883–3904 (2006).
- 320 60. Lowenstein, T. K., Timofeeff, M. N., Brennan, S. T., Hardie, L. A. & Demicco, R. V.



Oscillations in Phanerozoic seawater chemistry: Evidence from fluid inclusions. *Science* (80-. ). **294**, 1086–1088 (2001).

- 325 61. Horita, J., Zimmermann, H. & Holland, H. D. Chemical evolution of seawater during the Phanerozoic: Implications from the record of marine evaporites. *Geochim. Cosmochim. Acta* **66**, 3733–3756 (2002).
62. Chalk, T. B. *et al.* Causes of ice age intensification across the Mid-Pleistocene Transition. *Proc. Natl. Acad. Sci.* **114**, 13114–13119 (2017).
- 330 63. Foster, G. L., Lear, C. H. & Rae, J. W. B. The evolution of pCO<sub>2</sub>, ice volume and climate during the middle Miocene. *Earth Planet. Sci. Lett.* **341**, 243–254 (2012).
64. Greenop, R. *et al.* Orbital Forcing, Ice Volume, and CO<sub>2</sub> Across the Oligocene-Miocene Transition. *Paleoceanogr. Paleoclimatology* **34**, 316–328 (2019).
65. Sosdian, S. M., Babila, T. L., Greenop, R., Foster, G. L. & Lear, C. H. Ocean Carbon  
335 Storage across the middle Miocene: a new interpretation for the Monterey Event. *Nat. Commun.* **11**, 1–11 (2020).
66. Evans, D. & Müller, W. Deep time foraminifera Mg/Ca paleothermometry: Nonlinear correction for secular change in seawater Mg/Ca. *Paleoceanography* **27**, (2012).
67. Tierney, J. E., Malevich, S. B., Gray, W., Vetter, L. & Thirumalai, K. Bayesian calibration  
340 of the Mg/Ca paleothermometer in planktic foraminifera. *Paleoceanogr. Paleoclimatology* (2019).
68. Anand, P., Elderfield, H. & Conte, M. H. Calibration of Mg/Ca thermometry in planktonic foraminifera from a sediment trap time series. *Paleoceanography* **18**, (2003).
69. Gray, W. R. *et al.* Deglacial upwelling, productivity and CO<sub>2</sub> outgassing in the North  
345 Pacific Ocean. *Nat. Geosci.* **11**, 340–344 (2018).

70. Lemarchand, D., Gaillardet, J., Lewin, E. & Allegre, C. J. Boron isotope systematics in large rivers: implications for the marine boron budget and paleo-pH reconstruction over the Cenozoic. *Chem. Geol.* **190**, 123–140 (2002).
71. Simon, L., Lécuyer, C., Maréchal, C. & Coltice, N. Modelling the geochemical cycle of boron: Implications for the long-term  $\delta^{11}\text{B}$  evolution of seawater and oceanic crust. *Chem. Geol.* **225**, 61–76 (2006).
72. Greenop, R. *et al.* A record of Neogene seawater  $\delta^{11}\text{B}$  reconstructed from paired  $\delta^{11}\text{B}$  analyses on benthic and planktic foraminifera. *Clim. Past* **13**, 149–170 (2017).
73. Klochko, K., Kaufman, A. J., Yao, W., Byrne, R. H. & Tossell, J. A. Experimental measurement of boron isotope fractionation in seawater. *Earth Planet. Sci. Lett.* **248**, 276–285 (2006).
74. Shields, C. A. *et al.* The low-resolution CCSM4. *J. Clim.* **25**, 3993–4014 (2012).
75. Dowsett, H. J. *et al.* Sea surface temperature of the mid-Piacenzian ocean: a data-model comparison. *Sci. Rep.* **3**, (2013).
76. Brierley, C., Burls, N., Ravelo, C. & Fedorov, A. Pliocene warmth and gradients. *Nat. Geosci.* **8**, 419–420 (2015).
77. Moore, J. K., Doney, S. C. & Lindsay, K. Upper ocean ecosystem dynamics and iron cycling in a global three-dimensional model. *Global Biogeochem. Cycles* **18**, (2004).
78. Blanke, B. & Raynaud, S. Kinematics of the Pacific equatorial undercurrent: An Eulerian and Lagrangian approach from GCM results. *J. Phys. Oceanogr.* **27**, 1038–1053 (1997).
79. Gent, P. R. & McWilliams, J. C. Isopycnal mixing in ocean circulation models. *J. Phys. Oceanogr.* **20**, 150–155 (1990).
80. Van Sebille, E. *et al.* Lagrangian ocean analysis: Fundamentals and practices. *Ocean*

*Model.* **121**, 49–75 (2018).

- 370 81. Arakawa, A. & Lamb, V. R. Computational design of the basic dynamical processes of the  
UCLA general circulation model. *Gen. Circ. Model. Atmos.* **17**, 173–265 (1977).
82. Bartoli, G., Hönlisch, B. & Zeebe, R. E. Atmospheric CO<sub>2</sub> decline during the Pliocene  
intensification of Northern Hemisphere glaciations. *Paleoceanography* **26**, (2011).
83. Hönlisch, B., Hemming, N. G., Archer, D., Siddall, M. & McManus, J. F. Atmospheric  
375 carbon dioxide concentration across the mid-Pleistocene transition. *Science* (80-. ). **324**,  
1551–1554 (2009).
84. Seki, O. *et al.* Alkenone and boron-based Pliocene pCO<sub>2</sub> records. *Earth Planet. Sci. Lett.*  
**292**, 201–211 (2010).
85. Sosdian, S. M. *et al.* Constraining the evolution of Neogene ocean carbonate chemistry  
380 using the boron isotope pH proxy. *Earth Planet. Sci. Lett.* **498**, 362–376 (2018).
86. de la Vega, E., Chalk, T. B., Wilson, P. A., Bysani, R. P. & Foster, G. L. Atmospheric CO  
2 during the Mid-Piacenzian Warm Period and the M2 glaciation. *Sci. Rep.* **10**, 1–8  
(2020).
87. Fairbanks, R. G., WIEBE, P. H. & Bé, A. W. H. Vertical distribution and isotopic  
385 composition of living planktonic foraminifera in the western North Atlantic. *Science* (80-.  
). **207**, 61–63 (1980).
88. Fairbanks, R. G., Sverdlöve, M., Free, R., Wiebe, P. H. & Bé, A. W. H. Vertical  
distribution and isotopic fractionation of living planktonic foraminifera from the Panama  
Basin. *Nature* **298**, 841–844 (1982).
- 390 89. Delaney, M. L., Bé, A. W. H. & Boyle, E. A. Li, Sr, Mg, and Na in foraminiferal calcite  
shells from laboratory culture, sediment traps, and sediment cores. *Geochim. Cosmochim.*

*Acta* **49**, 1327–1341 (1985).

90. Kim, J.-H. *et al.* New indices and calibrations derived from the distribution of crenarchaeal isoprenoid tetraether lipids: Implications for past sea surface temperature

395 reconstructions. *Geochim. Cosmochim. Acta* **74**, 4639–4654 (2010).

91. Müller, P. J., Kirst, G., Ruhland, G., Von Storch, I. & Rosell-Melé, A. Calibration of the alkenone paleotemperature index U37K' based on core-tops from the eastern South Atlantic and the global ocean (60° N-60° S). *Geochim. Cosmochim. Acta* **62**, 1757–1772 (1998).

- 400 92. Dekens, P. S., Lea, D. W., Pak, D. K. & Spero, H. J. Core top calibration of Mg/Ca in tropical foraminifera: Refining paleotemperature estimation. *Geochemistry, Geophys. Geosystems* **3**, 1–29 (2002).

405

410

**Figures:**

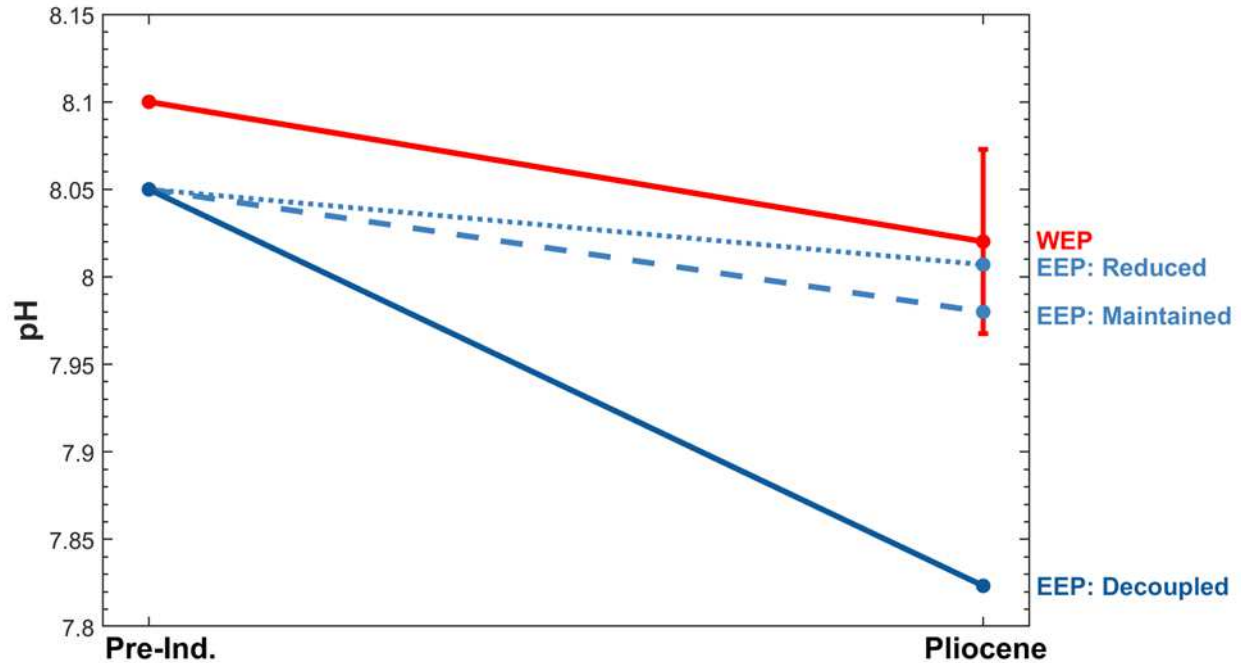


**Fig. 1. Alternative hypotheses for surface pH in the western and eastern equatorial Pacific, 0-6Ma.** The strength of the east-west pH gradient is hypothesized to have been different in the Miocene/Pliocene than it is today, depending on dynamics dominating the climate system at that time. **Red line:** Pre-Industrial pH for the western equatorial Pacific (WEP) ( $\sim 8.1$ )<sup>31</sup> and pH from  $\sim 6$ Ma ( $\sim 8.02$ , the average  $\delta^{11}\text{B}$ -derived result of this study from  $\sim 6$ Ma at site ODP 806, with 2sd error bars). The blues represent three hypotheses for eastern equatorial Pacific (EEP) pH change relative to the pre-Industrial ( $\sim 8.05$ )<sup>31</sup>. **Blue dotted line:** coupled reduction in east-west temperature and pH gradients (i.e. same fractional change) during the Pliocene, with thermal gradient reduction as in Liu et al., 2019<sup>41</sup>. **Blue dashed line:** coupled reduction in Pliocene temperature and pH gradients (i.e. same fractional change), with a lesser reduction/maintained thermal gradient as in Zhang et al., 2014<sup>11</sup>. **Blue solid line:** decoupled changes in Pliocene temperature and pH gradients (i.e. pH gradient increased while thermal gradient reduced) as is predicted by the earth system model used in this study (output at 55m depth at location of site ODP 846 =  $\sim 7.82$ ).

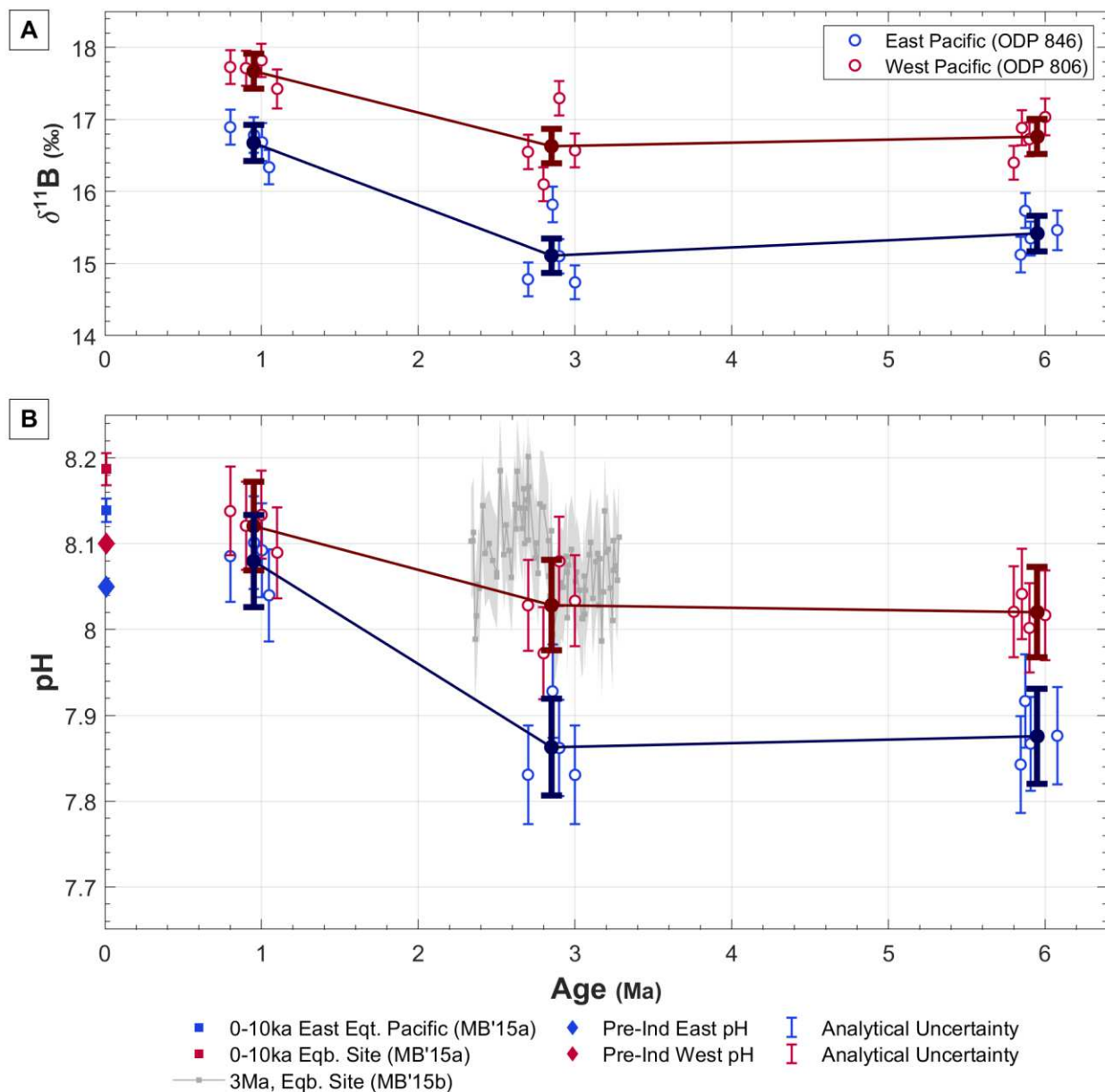


**Fig. 2. Western and Eastern Equatorial Pacific surface pH, 0-6Ma, from  $\delta^{11}\text{B}$  of planktonic foraminifera.** (A) The boron isotopic composition ( $\delta^{11}\text{B}$ ) of *O. universa* from sites ODP 846 (east, blue) and ODP 806 (west, red). Analytical uncertainty [ $2\sigma$ ] included as error bars and averages at ~1Ma, ~3Ma, and ~6Ma included as thickened, darkened points. (B)  $\delta^{11}\text{B}$ -derived pH for the same sites and time periods.  $2\sigma$  error bars produced by a Monte Carlo simulation ( $n = 10,000$  runs) including uncertainty on  $\delta^{11}\text{B}$ , the  $\delta^{11}\text{B}$  composition of seawater<sup>42</sup>, SST, and sea

surface salinity (SSS). Additional pH data included for reference are: pre-Industrial estimates for the eastern and western Pacific (diamonds)<sup>31</sup>; average pH over the last 10,000 years<sup>26</sup> from the eastern equatorial Pacific (blue square with 95% CIs, site ODP 1238) and from a site in  
440 equilibrium with the atmosphere (red square with 95% CIs, site PS 2498-1 in the southern Atlantic), and a mid-Pliocene ~3Ma equilibrium site<sup>43</sup> (grey points, ODP 999, central Caribbean with 95% CIs).

445

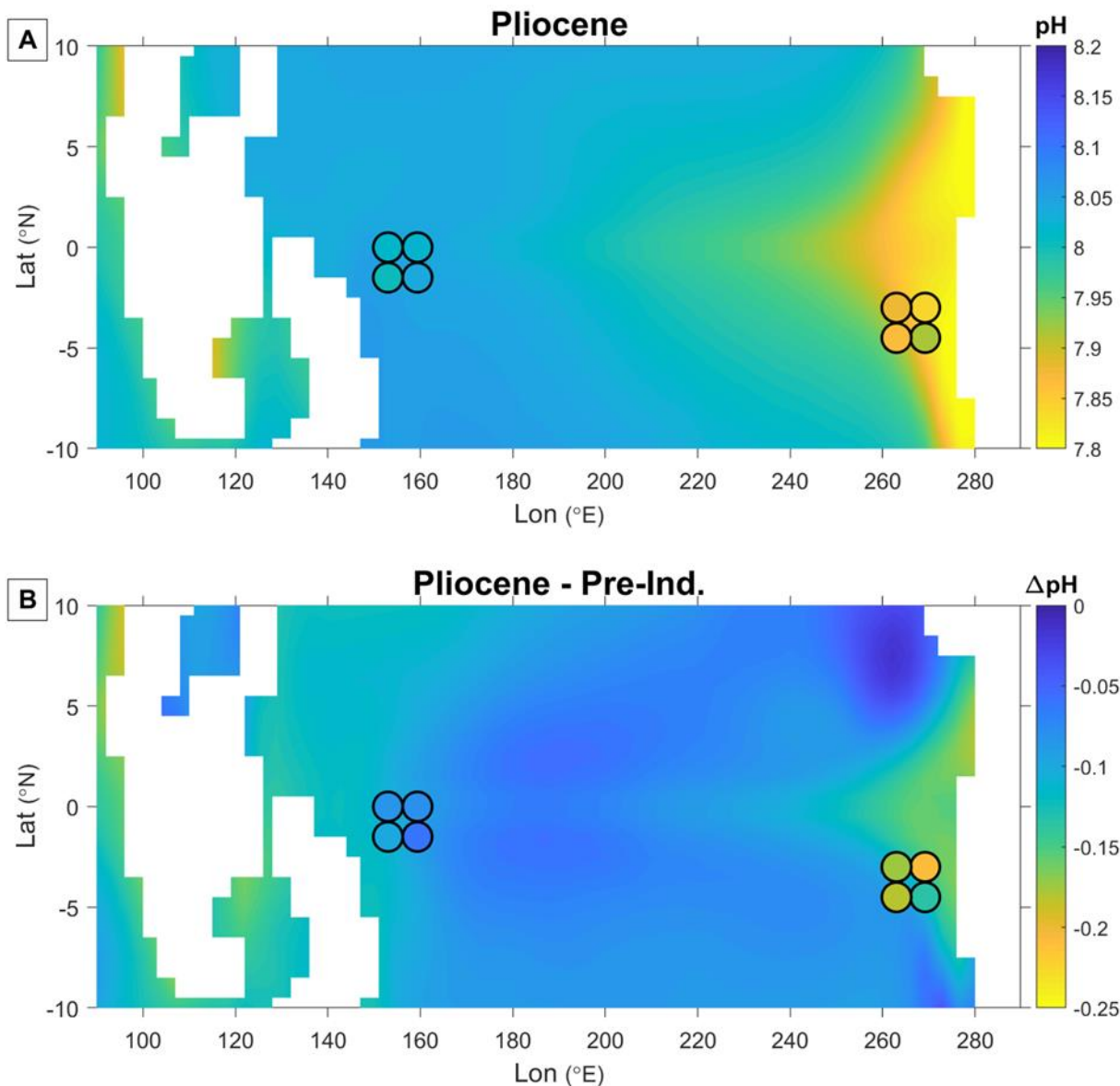


**Fig. 3. Model-Data comparison of pH at 55m depth.** (A) Climatological pH at 55m depth from the last 100 years of the Pliocene simulation (colored contours), overlaid with  $\delta^{11}\text{B}$ -derived pH values (colored circles) of ages ~5.7, ~5.8, ~5.9, and ~6.0Ma clockwise from the top right. More acidic waters are shown in yellow-green colors. (B) Same as (A) but depicting the difference in the Pliocene minus pre-Industrial control runs of the model (more acidic waters during the Pliocene shown in yellow-green colors). Colored circles show anomaly from the ~6.0Ma data to pre-Industrial pH from Feely et al., 2009<sup>31</sup>.



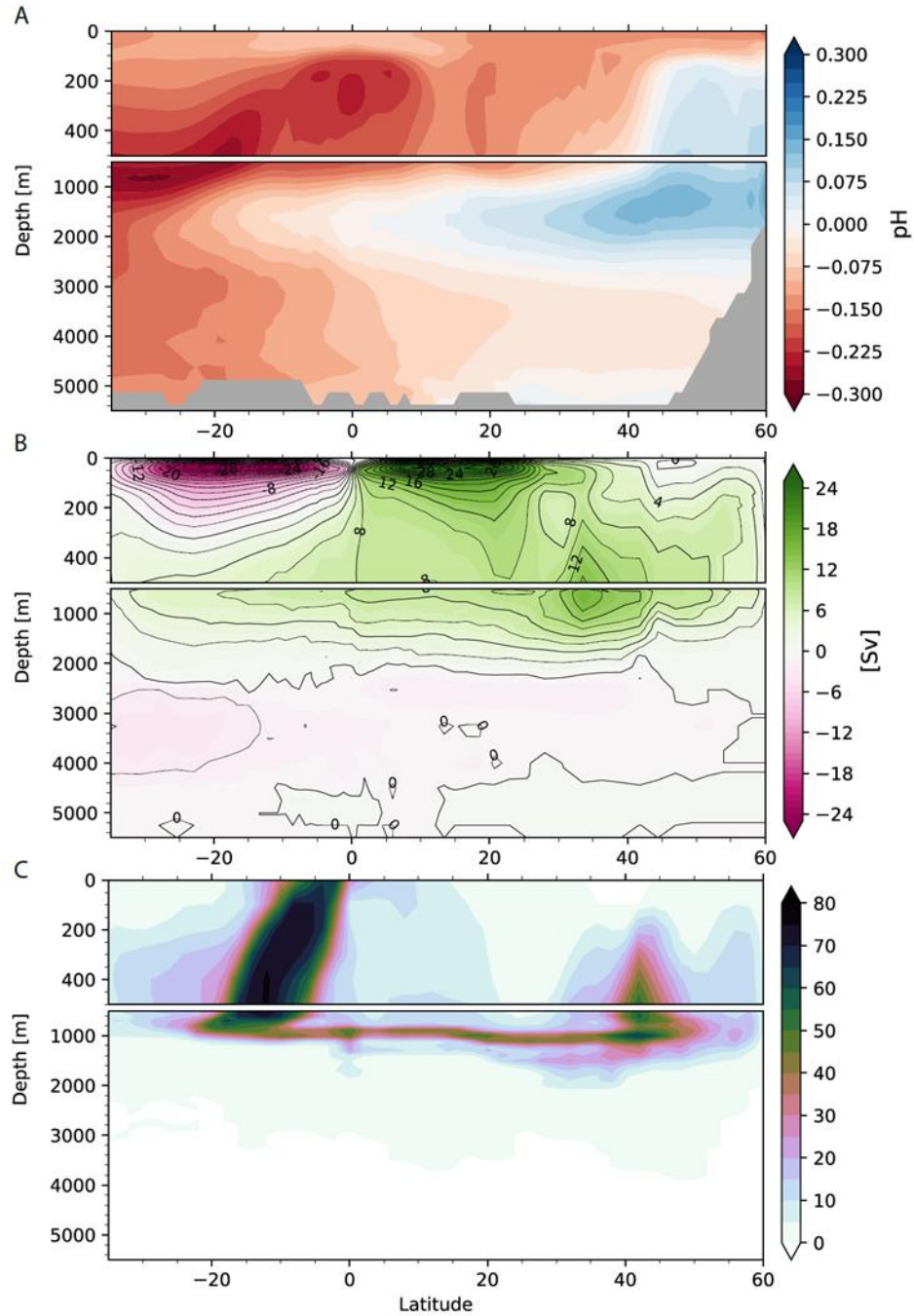


**Fig. 4. Model pH and water mass transport in the Pliocene Pacific.** (A) Zonally-averaged meridional transect of the pH anomaly (Pliocene minus preindustrial control), (B) Pliocene zonally-averaged stream function, and (C) latitude-depth pathways of water parcels sinking in the Pliocene subarctic North Pacific and upwelling in the tropical Pacific according to the Lagrangian

analysis. Pathways are depicted as the percentage number of parcels that enter each model grid cell and, in effect, show the density of parcel trajectories that connect the northern Pacific deep-water formation regions with the tropical ocean (see Materials and Methods in the Supplement for details of the Lagrangian analysis).

465

## Methods:

### *Study Sites and Species Selection*

To reconstruct the zonal pH gradient across the equatorial Pacific, samples were taken at ~3-million-year intervals from two sites in the eastern and western equatorial Pacific. The eastern  
470 site, ODP Site 846 (3° 5.7'S, 90° 49.1'W, water depth ~3300m), is located approximately 300km south of the Galapagos Islands near the convergence of the South Equatorial Current (SEC) and Peru Current and sits atop the Carnegie Ridge<sup>44</sup>. It sits in the central region of the east Pacific cold tongue and is subject to the strong upwelling of deep water that occurs there. The western site, ODP Site 806 (0° 19.1'N, 159° 21.7'E, water depth ~2500m) is located ~700km west of Papua  
475 New Guinea on the Ontong Java Plateau<sup>45</sup>. It is situated in the heart of the west Pacific warm pool, a region that is understood to be in equilibrium with the atmosphere with respect to CO<sub>2</sub><sup>25</sup>.

These sites have been the focus of numerous previous studies of the Pacific zonal SST gradient during the Pliocene<sup>1,2,5-7,9,11,46,47</sup>. A broad synthesis of this data and model simulations is presented in Fedorov et al., 2013 and 2015<sup>8,12</sup>. While several studies have sampled from site ODP  
480 Site 847 in the east Pacific<sup>1,6,9,47</sup>, we have elected to use samples from ODP Site 846 since this site, being slightly south of the equator, would likely be less affected by the formation of the Galapagos archipelago ~1.6Mya<sup>48</sup>. Samples from ODP Site 846 were taken from between 36 and 232 meters composite depth (mcd) and between 8 and 177 mcd at ODP Site 806.

The LR04 age model<sup>49</sup> was used for the eastern site ODP 846, while the western site ODP Site 806 use the age model of Zhang et al., 2017<sup>50</sup>, which is updated to the GTS 2004 timescale<sup>51</sup>. Although the planktonic foraminifera *Trilobatus sacculifer* (formerly *Globigerinoides sacculifer*<sup>52</sup>) has been the focal species in previous studies of a Pliocene Permanent El Niño<sup>1</sup>, they were not abundant enough in samples from ODP Site 846 for boron isotope analysis. In fact, ODP Site 846 assemblages were dominated by radiolarians with planktonic foraminifera making up only a small portion of the coarse fraction material. *Orbulina universa* was abundant enough, however, at both sites in the 300-355  $\mu\text{m}$  size fraction to pick the ~150-200 individuals needed for each  $\delta^{11}\text{B}$  measurement. Like *T. sacculifer*, *O. universa* makes its habitat in the mixed layer (~50-70m) where waters are well mixed and in communication with the atmosphere, and has been calibrated for boron isotopes<sup>37</sup>, making it a suitable candidate for this study of mixed layer pH<sup>36-38</sup>.

#### **Hypothesis Figure**

The schematic of Fig. 1 was generated by applying the same proportional reduction in the zonal thermal (SST) gradient (in the Pliocene relative to modern) as found by different studies to the modern-day zonal pH gradient. First, pre-Industrial pH for both the WEP and EEP was taken from Feely et al., 2009<sup>31</sup>. Next, a representative Miocene/Pliocene WEP pH (~8.02) was estimated from an equilibrium state with 400ppm atmospheric  $\text{CO}_2$  and a modern-like alkalinity (2275 mmol/kg) (alkalinity is understood to have been relatively invariant over the Cenozoic, staying close to modern values<sup>33</sup>, making this a robust assumption. Finally, for the dotted and dashed blue lines, a Miocene/Pliocene EEP pH was estimated from the reported reductions in the Pliocene zonal thermal (SST) gradient relative to modern as found by Liu et al., 2019,<sup>41</sup> (dotted line, an ~82% reduction) and Zhang et al., 2014,<sup>11</sup> (dashed line, a ~28% reduction). The percent-reduction in the zonal thermal gradient relative to modern as found by each of those studies was then applied

to the magnitude of the pre-Industrial zonal pH gradient ( $\sim 0.5$ )<sup>31</sup>, resulting in a Pliocene zonal pH gradient of either 0.014 (dotted line)<sup>41</sup> or 0.041 (dashed line)<sup>11</sup>. Pliocene EEP pH was estimated by applying those Pliocene pH gradients to the Pliocene WEP pH estimate ( $\sim 8.02$ ), resulting in  
510 Pliocene EEP pH values of  $\sim 8.006$  (dotted) and  $\sim 7.979$  (dashed). The solid blue line depicts the EEP pH put out by the earth system model used in this study in its Pliocene-like run ( $\sim 7.82$ ), which is interpreted to reflect a decoupling between Pliocene zonal thermal and pH gradients.

### ***Sample Preparation for Boron Isotope and Trace Elements Analysis***

Initial preparation of marine sediment samples involved disaggregating samples in sodium  
515 hexametaphosphate solution (2g/L) buffered with  $\text{NH}_4\text{OH}$ , washing in deionized water over a  $64\mu\text{m}$  sieve, and drying in a  $<50^\circ\text{C}$  oven. Samples were rewashed if the initial (or subsequent) wash cycle did not result in visually clean samples. Individuals of *O. universa* were picked from the  $300\text{--}355\mu\text{m}$  size range. Occasionally individuals from other size fractions were included (down to  $250\mu\text{m}$  and up to  $710\mu\text{m}$ , but rarely outside of the  $300\text{--}600\mu\text{m}$  range, see Table S1) if  
520 foraminifera were sparse, as the boron-pH calibration for *O. universa* has no statistically significant size trend within this range<sup>37</sup>. Sample sizes typically range from  $\sim 150\text{--}200$  foraminifera and  $\sim 2\text{--}4\text{ mg}$  of  $\text{CaCO}_3$ .

All subsequent laboratory procedures were carried out in a Picotrace class ten clean lab at the Yale Metal Geochemistry Center (Yale University) within an over-pressurized hood equipped  
525 with boron-free filters and using Milli-Q water ( $18.2\text{ M}\Omega$  with Q-Gard boron removal pack) and Teflon-distilled nitric acid ( $\text{HNO}_3$ ). Approximately  $\sim 2.5\text{ mg}$  of solid carbonate sample (i.e., the picked *Orbulina universa*) was cleaned following the procedure outlined in Foster et al., 2008,<sup>53</sup> and Rae et al., 2011,<sup>29</sup> and references therein. After lightly cracking open all individual chambers between clean glass slides, the solid sample was repeatedly ultrasonicated and rinsed with Milli-

530 Q water (5 x 30 seconds of ultrasonication) to remove clays. Organic matter was removed by  
subjecting the solid to oxidative cleaning using 250  $\mu\text{L}$  of 1%  $\text{H}_2\text{O}_2$  in 0.1 M  $\text{NH}_4\text{OH}$  at 80°C for  
3 x 5 minutes, with 15 seconds of ultrasonication in between. Afterwards, 250  $\mu\text{L}$  of 0.0005 M  
 $\text{HNO}_3$  was added to the solid for 30 seconds as a brief weak acid leach to remove any re-adsorbed  
contaminants. Samples were then rinsed twice with Milli-Q water. Finally, samples had 200  $\mu\text{L}$  of  
535 Milli-Q water added to them before incrementally adding 0.5 M  $\text{HNO}_3$  acid until the sample was  
totally dissolved (anywhere from 75 to 200  $\mu\text{L}$ ). The sample was centrifuged for 5 minutes to  
isolate any undissolved contaminant phases. A small aliquot (approximately 7% of the volume) of  
the resulting supernatant was transferred to an acid-cleaned plastic centrifuge tube for trace metal  
analysis, and the remaining supernatant was transferred to a Teflon beaker for isotope analysis.

540 Boron was separated from the dissolved carbonate matrix by passing the sample through  
pre-cleaned heat-shrunk Teflon micro-columns containing 20  $\mu\text{L}$  of ground, sieved (63-100  $\mu\text{m}$ )  
boron-specific anionic exchange resin, Amberlite IRA 743<sup>54</sup>, following the procedure of Foster et  
al., 2008<sup>53</sup>. Before performing column chemistry, the columns were cleaned by passing a full-  
column's volume of 0.5 M  $\text{HNO}_3$  plus 1mL of 0.5 M  $\text{HNO}_3$  plus 2 x 1mL of Milli-Q through each  
545 of the columns. Samples were also buffered prior to column chemistry with boron-clean sodium  
acetate (twice the volume of acid required to dissolve the solid sample) to maintain sample pH >  
5. The sample matrix was then rinsed through the columns by the addition of 10 x 160  $\mu\text{L}$  of Milli-  
Q water before being eluted with 5 x 120  $\mu\text{L}$  of 0.5 M  $\text{HNO}_3$  and collected in acid-cleaned Teflon  
beakers. Sample tails were also collected in separate Teflon beakers with a final elution of 1 x 120  
550  $\mu\text{L}$  of 0.5 M  $\text{HNO}_3$ . Each batch of columns included a JCp-1 carbonate geostandard (Japanese  
Geological Survey Porites Coral<sup>55</sup>) to monitor column performance and reproducibility, as well as

a total procedural blank (TPB) composed of 0.5 M HNO<sub>3</sub> and buffer to monitor cleanliness and potential sample contamination.

**Boron Isotope Analysis by MC-ICP-MS**

Boron isotope analysis was performed at the Yale Metal Geochemistry Center on a Thermo Finnigan<sup>TM</sup> Neptune Plus MC-ICP-MS equipped with 10<sup>12</sup> Ω resistors and tuned before analysis to optimize maximum <sup>11</sup>B/<sup>10</sup>B stability, following the procedure described of Foster et al., 2008,<sup>53</sup> and references therein. A Teflon barrel spray chamber and ammonia gas were used to optimize boron washout<sup>56</sup>.

Prior to analysis, boron concentration and potential contamination by the Na-rich buffer were checked in tails and in 20 µL aliquots of samples diluted with 100 µL of 0.5M HNO<sub>3</sub>. Tails typically made up <1% of the boron loaded. Depending on the sample size, boron isotope samples range from ~5–13 ng, yielding solutions for analysis of ~8–21 ppb (ng/g).

Samples were bracketed with 50 ppb NIST SRM 951 boric acid standard, which was used to correct for machine-induced mass-fractionation and convert <sup>11</sup>B/<sup>10</sup>B ratios to delta notation. To monitor accumulating blank contamination from the laboratory atmosphere while the vials were open for analysis, a blank consisting of the same volume of 0.5 M HNO<sub>3</sub> as the samples (600 µL) was analyzed every third sample and used to correct sample δ<sup>11</sup>B values. Samples were measured in duplicate, with the mean δ<sup>11</sup>B being reported.

The average blank contribution from the total procedural blank (TPB) included in each batch of columns was ~19 pg (~0.15% of average sample size). Sample δ<sup>11</sup>B values were corrected using TPB δ<sup>11</sup>B values. The average blank correction (δ<sup>11</sup>B<sub>original</sub> – δ<sup>11</sup>B<sub>corrected</sub>) was ~0.011‰ and therefore below typical measurement uncertainty.

The uncertainty of boron isotope measurements ( $2\sigma$  was typically 0.24‰) was determined  
575 from a relationship between signal size and external reproducibility:

$$2\sigma = 8.67 * \exp(-42.21[^{11}\text{B}]) + 0.28 * \exp(-0.21[^{11}\text{B}]) \quad (\text{Eqn. 1})$$

where  $[^{11}\text{B}]$  is the  $^{11}\text{B}$  signal intensity in volts. This relationship is derived from repeat analysis of multiple batches of roughly mass-matched JCp-1 pass through columns with individual sample batches. For this study, the average  $\delta^{11}\text{B}$  value of JCp-1 was  $24.18 \pm 0.23\text{‰}$  ( $2\sigma$ ) ( $n = 8$ ).

### 580 *Trace Element Analysis by ICP-MS*

Trace element analysis was performed at the Yale Metal Geochemistry Center on a Thermo Finnigan <sup>TM</sup> Element XR ICP-MS, again using a Teflon barrel spray chamber and ammonia gas and following the procedure outlined in Foster et al., 2008,<sup>53</sup> and references therein. In-house consistency standards (SMEG) were analyzed to monitor machine behavior. Sample matrix was  
585 matched to the  $[\text{Ca}]$  of bracketing standards to optimize reproducibility and analyzed for a full suite of trace elements (e.g. Ca, Mg, Sr, Na, Mn, Li, B, Ba, Cd, U, Al, Cu, Fe, Nd and Zn).

### *Calculation of Mg/Ca SSTs*

Planktonic foraminiferal Mg/Ca was measured on an aliquot of each  $\delta^{11}\text{B}$  sample and used to estimate SSTs in order to accurately calculate pH from  $\delta^{11}\text{B}$ . Given the residence times of  
590 magnesium ( $\sim 13$  Myr)<sup>57</sup> and calcium ( $\sim 1$  Myr)<sup>58</sup> in seawater, the Mg/Ca composition of seawater ( $\text{Mg}/\text{Ca}_{\text{sw}}$ ) is likely to have varied on timescales of  $\sim 1$ -10 Myr. We therefore account for secular change in  $\text{Mg}/\text{Ca}_{\text{sw}}$  using the  $\text{Mg}/\text{Ca}_{\text{sw}}$  record of Fantle and DePaolo, 2006<sup>59</sup>. This record is based on the Mg concentration of pore fluid and closely matches estimates for the Pliocene from halite fluid inclusions<sup>60,61</sup>. In using the  $\text{Mg}/\text{Ca}_{\text{sw}}$  record of Fantle and DePaolo, 2006,<sup>59</sup> we follow the  
595 lead of other boron-based studies of the Plio-Pleistocene<sup>43,62</sup>. Similarly, the  $\text{Mg}/\text{Ca}_{\text{sw}}$  record of

Horita et al., 2002,<sup>61</sup> has been used in a number of previous boron-based studies set in the Miocene<sup>63–65</sup>.

We do not, however, account for the non-linear response of foraminiferal Mg/Ca to changing Mg/Casw outlined by Evans and Müller, 2012,<sup>66</sup> who show that  $\frac{Mg}{Ca_{test}} \propto$

$$600 \quad \left( \frac{\frac{Mg^{t=t}}{Ca_{SW}}}{\frac{Mg^{t=0}}{Ca_{SW}}} \right)^H \text{ where } 0 < H < 1 \text{ and “t=0” refers to modern Mg/Casw (5.2 mol/mol)}^{33} \text{ and “t=t” refers}$$

to Mg/Casw at different points in Earth’s past. The primary reason for this is that a coefficient of non-linearity (“H” in Evans and Müller, 2012,<sup>66</sup> has not yet been calibrated for *O. universa*. While this choice of procedure results in lower SSTs than had the power-law relationship been assumed or the new Bayesian calibration of Tierney et al., 2019,<sup>67</sup> been employed (Fig. S6), we demonstrate  
605 in Figs. S7 and S8 that this choice does not affect the conclusions of this study.

In the main text figures and analyses, SSTs are calculated from planktonic foraminiferal Mg/Ca using the *O. universa* species-specific calibration of Anand et al., 2003,<sup>68</sup> ( $A = 0.090$ ,  $B = 0.595$  for  $Mg/Ca = B \cdot \exp^{AT}$ ), correcting for Mg/Casw using the record of Fantle and DePaolo, 2006,<sup>59</sup> and assuming a linear relationship between  $Mg/Ca_{test}$  and  $Mg/Casw$  (i.e.  $H = 1$  in  $\frac{Mg}{Ca_{test}} =$

$$610 \quad \left( \frac{\frac{Mg^{t=t}}{Ca_{SW}}}{\frac{Mg^{t=0}}{Ca_{SW}}} \right)^H B \exp^{AT}.$$

### ***pH and pCO<sub>2</sub> Estimates from Boron Isotopes***

Calculation of pH from  $\delta^{11}B$  was performed using the *O. universa* calibration of Henahan et al., 2016<sup>37</sup>. Because of the complexity of this calculation and the multiple sources of uncertainty to be incorporated, a Monte Carlo approach was used to estimate uncertainty, following the  
615 example of numerous previous boron-pH studies<sup>26,43,62,63,69</sup> and using a previously-published Monte Carlo simulation code<sup>30</sup>. Reported pH values are the mean of 10,000 replicates of a Monte



Carlo simulation in which the involved parameters (sea surface temperature, sea surface salinity (SSS),  $\delta^{11}\text{B}_{\text{calcite}}$ , and  $\delta^{11}\text{B}_{\text{sw}}$ , and alkalinity (for the purposes of calculating  $\text{pCO}_2$ )) are randomly generated from within either a normal or uniform frequency distribution spanning the uncertainty  
620 surrounding each parameter. Following the example of Chalk et al., 2017,<sup>62</sup>, we place normal distributions around SST, SSS,  $\delta^{11}\text{B}_{\text{calcite}}$ , and  $\delta^{11}\text{B}_{\text{sw}}$  and a uniform distribution spanning a generous range ( $\pm 200$  mmol/kg) around alkalinity.

SSTs fed into the Monte Carlo simulations were derived from Mg/Ca data described in the “Calculation of Mg/Ca SSTs” section and, unlike other proxy data, a wider and more conservative  
625 range of uncertainty of  $\pm 2^\circ\text{C}$  is applied instead of the root sum of squares of the analytical and calibration uncertainty (which was small,  $< \sim 0.9^\circ\text{C}$ ). Uncertainty around  $\delta^{11}\text{B}_{\text{calcite}}$  is the reported analytical uncertainty ( $2\sigma$ ). Because the residence time of boron in seawater is believed to be on the order of 10-20 Myr<sup>70-72</sup>, the modern-day value of  $\delta^{11}\text{B}_{\text{sw}}$  with its reported uncertainty ( $39.61 \pm 0.04\text{‰}$  ( $2\sigma$ )) is used here<sup>42</sup>. A generous range of sea surface salinity around a representative  
630 modern-day value is applied:  $34.5 \pm 1$  psu. Reported uncertainty on pH is one standard deviation of the 10,000 simulated pH values. For the purpose of calculating  $\text{pCO}_2$  estimates from the pH values, a modern-like value of alkalinity (2275 mmol/kg) was applied with a generous range of uncertainty ( $\pm 200$  mmol/kg). Alkalinity is understood to have remained relatively constant over the Cenozoic<sup>33</sup>, making this a more robust assumption than, for instance, the assumption of a  
635 modern-like calcite saturation state (although this gives similar results, Fig. S2).

### ***Effect of SST Estimates on pH Reconstructions***

To calculate pH, SSTs were estimated from planktonic foraminiferal calcite Mg/Ca using the *O. universa*-specific calibration of Anand et al., 2003,<sup>68</sup> and corrected for the Mg/Ca composition of seawater using the  $\text{Mg}/\text{Ca}_{\text{sw}}$  record of Fantle and DePaolo, 2006<sup>59</sup>. These are

640 plotted against a compilation of previously published SST records for these and nearby sites in Fig. S9.

The relatively low SSTs we report in the west relative to other previously reported records (Fig. S9) might reflect choice of Mg/Ca<sub>sw</sub> record. The inconsistency is not driven by the use of a linear instead of power-law seawater correction<sup>66</sup>, as the power-law correction would result in only slightly higher SSTs (Fig. S6) than those reported here. In addition, a power-law correction would affect the eastern and western data points equivalently, and our eastern data points seem in line with previous records using the linear Mg/Ca correction. The low SSTs we report in the west could reflect our choice of foraminiferal species as well. Previous Mg/Ca SST records<sup>1</sup> reported in Fig. S9 are derived from *T. sacculifer*, whose depth habitat is still in the mixed layer but on average slightly shallower than that of *O. universa* (~40-50 m versus ~50-70 m)<sup>36-38</sup>. However, again we would expect this effect to affect our eastern and western data points equally, and our eastern points are roughly in line with previously published records.

Fortunately, the fractionation of boron into foraminiferal calcite and thus the calculation of pH from  $\delta^{11}\text{B}$  is relatively insensitive to temperature<sup>29,53,73</sup>, as demonstrated in Figs. S7 and S8. These figures show pH estimates changing by ~0.01-0.05 depending of choice of temperature input (i.e., Mg/Ca using a linear correction for Mg/Ca<sub>sw</sub>, Mg/Ca using a power-law correction for Mg/Ca<sub>sw</sub>, or the TEX86 SST record of Zhang et al., 2014,<sup>11</sup> see Fig. S7). The range of possible pH values produced by different SST proxies increases going back in time at SST records diverge more and more but still rarely surpasses ~0.05 in our data (Fig. S8). Similarly, calculating pH using the SSTs derived from the BAYMAG calibration<sup>67</sup> (Fig. S10)—while shifting pH values down ~0.05 at the 3Ma and 6Ma time points—does not affect the main conclusions of this study.

### ***Physical and Biogeochemical Modelling***

Numerical simulations were performed using the National Center for Atmospheric Research (NCAR)'s coupled ocean-atmosphere Community Earth System Model (CESM) version 1.0.4, with the T31 gx3v7 configuration designed for long-term paleoclimate simulations<sup>74</sup>. The atmospheric and land surface components (the Community Atmosphere Model 4 and Community Land Model 4) have a spectral truncation of T31, and the oceanic and sea ice components (POP2 and Community Ice Code) has a resolution ranging from 3° near the poles to 1° at the equator. Three simulations have been performed, a preindustrial control simulation and two Pliocene-like experiments designed to reproduce the magnitude and spatial structure of the large-scale warming patterns, specifically the reduction in the meridional SST gradient, seen in Pliocene SST reconstructions<sup>8,12,75,76</sup>. All three experiments have the biogeochemical model enabled<sup>77</sup> allowing us to evaluate the impact of the simulated changes in ocean temperature, salinity and circulation on ocean pH. All three simulations have been run for 3000 years, allowing the system to reach near-equilibrium. The analysis presented here is based on the climatology of the last 100 years of each simulation (years 2900-3000), and Pliocene anomalies are reported relative the preindustrial control run.

We refer to the two Pliocene-like experiments as Experiment A & B respectively. The experimental design for Experiment A (on which the central analysis presented here is based, i.e. Figs. 3, 4, S3) is similar to that of the Early Pliocene-like simulation evaluated in Burls et al., 2017,<sup>16</sup> and Burls et al., 2014a, 2014b,<sup>34,35</sup> but with an active biogeochemical component. For full details, see Burls et al., 2014a, 2014b,<sup>34,35</sup>. Briefly, mean cloud albedo is reduced in the extratropics and increased in the tropics by altering the liquid and ice water path in the shortwave radiation scheme in different latitudinal bands. All other elements of the climate system remain unaltered and are allowed to evolve freely in response to the ocean's and atmosphere's adjustments to the

imposed changes in cloud shortwave radiative forcing (note that while CO<sub>2</sub> in Exp. A was set to 280ppm in the atmospheric component and the global warming is instead supported by the cloud albedo changes and the associated water vapor feedback, atmospheric CO<sub>2</sub> was set to 400ppm in the ocean biogeochemistry (BGC) component). Relatively good agreement with available proxy SST data for the Early Pliocene is seen for this configuration<sup>34</sup>. As presented in Burls et al., 2017,<sup>16</sup> a Pacific meridional overturning circulation (PMOC) develops after some 1500 years of computation (Fig. S5C) due to an erosion of the North Pacific halocline – a result of the hydrological cycle response to the weakened large-scale SST gradient that leads to the weakening of atmospheric water vapor transport to the subarctic North Pacific. A secondary Pliocene-like experiment, Experiment B, is a hybrid experiment in which both an altered cloud albedo gradient and 400ppmv CO<sub>2</sub> in the atmosphere act to induce Pliocene-like SSTs. For Experiment B the liquid water path was reduced poleward of 15°N & 15°S by 50% while the ice and liquid water paths were increased equatorward of 15°N & 15°S by 240%, as compared to Experiment A in which the liquid water path was reduced poleward of 15°N & 15°S by 60% while the ice and liquid water paths were increased equatorward of 15°N & 15°S by 240%. A slightly stronger meridional temperature gradient and a slightly weaker shallower PMOC than that of Experiment A develops (Fig. S5E). Of note, the response of large-scale SST gradients in climate models to Pliocene CO<sub>2</sub> forcing alone (~400ppm) is too weak, hence the introduction of altered cloud albedo gradients that allow a reduction of the meridional SST gradient comparable to the observed. For further details see Fedorov et al., 2015<sup>12</sup>. In terms of pH, Experiment A and Experiment B both support the main conclusions of this paper (compare Fig. 4 and Fig. S11).

### ***Lagrangian Analysis of Water Parcel Trajectories***

Water parcel trajectories were modeled in order to identify both the surface source regions of deep water formation in the North Pacific and the mixed layer destinations where that water re-surfaces, determined according to a Lagrangian ocean analysis approach that tracks water parcels in the Pacific Ocean of the CESM climate model (see above for model description). This analysis was performed using the Ariane software package<sup>78</sup> which models water parcel trajectories by time-integrating velocity fields output by the ocean model. Trajectories calculated from ocean model momentum equations in this way—when coupled with a parameterization for subgrid-scale eddy-induced velocities (EIVs)<sup>79</sup>—depict the purely advective pathways of water parcels/tracers (i.e. without the effect of diffusion). To resolve the long residence timescales of PMOC water in the deep ocean, particles were allowed to loop continuously over the 100 years of model output (see Van Sebille et al., 2018,<sup>80</sup> for a discussion on particle looping).

Model tracer particles were seeded in every grid cell of the Pacific Ocean basin at 25°N and at every timestep (~1 million particles) before being integrated both backwards in time (to identify the particle mixed layer source regions at high northern latitudes) and forwards in time (to identify their mixed layer destinations). Time-integration in both cases was stopped when particles reached the model mixed layer. Particles found to originate close to the northern margin of the Pacific Ocean basin (north of ~40°N), clearly identifiable as PMOC water that is separate from the subtropical sources of the shallow wind-driven cells, were then isolated and subsequently run forwards in time from their original starting positions at 25°N. Of these, the particles that upwelled into the tropical Pacific (approximately 10% of them) were then further identified and their pathways and timescales analyzed.

Because the CESM ocean model used in this study is configured on an Arakawa B-grid, ocean model velocities had to first be linearly interpolated onto a C-grid configuration<sup>81</sup> in order

to be compatible with the Ariane software. EIV values also had to be set to zero at the ocean boundary to prevent unrealistic propagation of particles, however the Pacific Ocean domain was found to be minimally affected by this problem, and results overall were only weakly sensitive to it.

### 735 ***Data Availability***

The data generated and analyzed in this study are included in this published article and in its supplementary Extended Data section.

### **Acknowledgements:**

740 The authors acknowledge and appreciate the aid of Jamie Robbins, Wayne Strojie, Dan Asael, and Shuang Zhang in supervising clean lab chemistry, boron and trace element analysis, and data processing. The authors also appreciate discussion with James Rae concerning the Monte Carlo simulation used in this study. This work was supported by NSF Award 1602557 and 170251 to PMH, NSF Award 1844380 to NJB and a Sloan Ocean Fellowship to PMH & NJB. Additional  
745 funding to AVF was provided by the Guggenheim Fellowship and the ARCHANGE project (ANR-18-MPGA-0001, France). We acknowledge high-performance computing support from Cheyenne (<https://doi.org/10.5065/D6RX99HX>) provided by NCAR's Computational and Information Systems Laboratory, sponsored by the NSF.

### 750 **Author Contributions:**

MS: boron and trace element data collection, data analysis, writing, editing. NB: model simulations, writing, editing. PJ: model simulations, supervision. AF: supervision, writing, editing. MT: model simulations, Lagrangian analysis, editing. DP: data processing, supervision, editing.

HF: BAYMAG SST data processing, supervision, editing. NP: conceptualization, supervision,  
755 writing, editing. PH: conceptualization, supervision, writing, editing.

### **Competing Interest Declaration:**

The authors declare no competing interests.

### **760 Additional Information:**

Correspondence and requests for materials should be addressed to Dr. Pincelli Hull  
([pincelli.hull@yale.edu](mailto:pincelli.hull@yale.edu)) and Madison Shankle ([mgs23@st-andrews.ac.uk](mailto:mgs23@st-andrews.ac.uk)).

765

770

775

### **Extended Data and Figures**

**Table S1. Size fractions of *O. universa* making up samples.**

Light grey shading shows the size fractions making up the majority (>50%) of total count of each sample.

Sample	East or West Pacific	Age (Ma)	Total Count	Total Mass (mg)	250-300 µm	300-355 µm	355-425 µm	425-500 µm	500-600 µm	600-710 µm	710-850 µm	> 850 µm
MS 63	W	0.800	90	3.24				28	50	12		
MS 62	W	0.900	115	3.423				30	85			
MS 61	W	1.000	334	3.8				72	147	65	43	7
MS 60	W	1.100	57	3.236				7	24	14	12	
MS 55	W	2.700	65	3.405				22	32	9	1	1
MS 56	W	2.800	74	3.576			9	12	35	13	5	
MS 57	W	2.900	79	3.241			14	12	21	14	14	4
MS 58	W	3.000	81	3.597		7	2	12	34	12	12	2
MS 45	W	5.800	80	3.497		12	22	17	23	5	1	
MS 52	W	5.852	130	3.552	15	37	48	22	7	1		
MS 46	W	5.899	99	4.634		2	10	49	26	8	4	
MS 51	W	6.000	105	2.606	2	15	40	33	14	1		
MS 43	E	0.800	193	2.3		193						
MS 42	E	0.952	183	2.4		183						
MS 41	E	1.003	126	1.3		126						
MS 40	E	1.048	185	2.5		185						
MS 53	E	2.700	290	3.621		167	123					
MS 64	E	2.856	89	2.127	9	22	15	14	28	1		
MS 54	E	2.900	238	3.171		98	140					
MS 59	E	3.000	271	3.973	11	45	91	88	31	5		
MS 49	E	5.844	185	2.348	82	56	31	11	5			
MS 50	E	5.873	309	2.414	192	73	31	8	4		1	
MS 48	E	5.907	389	3.462	254	52	67	13	3			
MS 47	E	6.077	244	2.263	160	14	58	11	1			

780

785



**Table S2. Mg/Ca Data and SST Estimates.**

Mg/Ca ratios measured on the samples of *O. universa* in this study and the SST estimates resulting from the calibration of Anand et al., 2003,<sup>68</sup> correcting for Mg/Ca<sub>sw</sub> using the record of Fantle and DePaolo, 2006,<sup>59</sup> and assuming a linear relationship between Mg/Ca<sub>test</sub> and Mg/Ca<sub>sw</sub>. Note (\*), the data point for MS45 was lost, and so an SST was generated for this point by linear extrapolation from the SSTs of the two subsequent samples (MS52 and MS46).

Sample ID	East or West Pacific	Age (Ma)	Mg/Ca (mmol/mol)	SST (°C)
MS63	W	0.800	5.109	24.9
MS62	W	0.900	5.722	26.3
MS61	W	1.000	5.521	26.0
MS60	W	1.100	5.804	26.8
MS55	W	2.700	4.488	24.9
MS56	W	2.800	4.709	25.7
MS57	W	2.900	4.893	26.6
MS58	W	3.000	3.928	24.6
MS45*	W	5.800		24.3*
MS52	W	5.852	3.793	26.6
MS46	W	5.899	3.966	28.7
MS51	W	6.000	4.607	30.0
MS43	E	0.800	4.252	22.9
MS42	E	0.952	3.423	20.6
MS41	E	1.003	3.369	20.6
MS40	E	1.048	3.829	22.0
MS53	E	2.700	4.245	24.3
MS64	E	2.856	5.109	26.9
MS54	E	2.900	4.314	25.2
MS59	E	3.000	3.647	23.8
MS49	E	5.844	4.006	27.1
MS50	E	5.873	3.905	27.0
MS48	E	5.907	3.924	27.5
MS47	E	6.077	3.677	27.8

**Data S2.  $\delta^{11}\text{B}$  Data and pH/pCO<sub>2</sub> Estimates.**

$\delta^{11}\text{B}$  measured on the samples of *O. universa* in this study (with analytical uncertainty, two standard deviations) and the pH estimates resulting from the Monte Carlo simulation (with two standard deviations from n = 10,000 runs, see Materials and Methods for details of the Monte Carlo simulation).

Sample ID	East or West Pacific	Age (Ma)	$\delta^{11}\text{B}$ (‰)	2sd $\delta^{11}\text{B}$ (‰)	pH	2sd pH	pCO <sub>2</sub> (ppm)	2sd pCO <sub>2</sub> (ppm)
MS63	W	0.800	17.73	0.24	<b>8.12</b>	0.020	316	45
MS62	W	0.900	17.71	0.24	<b>8.13</b>	0.020	330	47
MS61	W	1.000	17.82	0.23	<b>8.14</b>	0.020	318	45
MS60	W	1.100	17.43	0.27	<b>8.11</b>	0.020	361	53
MS55	W	2.700	16.55	0.24	<b>8.01</b>	0.020	432	64
MS56	W	2.800	16.10	0.24	<b>7.94</b>	0.020	504	75
MS57	W	2.900	17.30	0.24	<b>8.07</b>	0.020	372	53
MS58	W	3.000	16.57	0.24	<b>8.00</b>	0.020	426	63
MS45	W	5.800	16.40	0.24	<b>7.97</b>	0.020	442	66
MS52	W	5.852	16.88	0.24	<b>8.02</b>	0.020	415	60
MS46	W	5.899	16.73	0.23	<b>8.00</b>	0.020	461	66
MS51	W	6.000	17.03	0.26	<b>8.03</b>	0.020	440	64
MS43	E	0.800	16.89	0.25	<b>8.11</b>	0.020		
MS42	E	0.952	16.78	0.25	<b>8.11</b>	0.020		
MS41	E	1.003	16.68	0.26	<b>8.11</b>	0.020		
MS40	E	1.048	16.34	0.24	<b>8.07</b>	0.020		
MS53	E	2.700	14.78	0.24	<b>7.86</b>	0.030		
MS64	E	2.856	15.82	0.25	<b>7.97</b>	0.020		
MS54	E	2.900	15.10	0.24	<b>7.87</b>	0.030		
MS59	E	3.000	14.74	0.24	<b>7.85</b>	0.030		
MS49	E	5.844	15.12	0.24	<b>7.85</b>	0.030		
MS50	E	5.873	15.73	0.24	<b>7.92</b>	0.020		
MS48	E	5.907	15.35	0.23	<b>7.89</b>	0.020		
MS47	E	6.077	15.46	0.28	<b>7.91</b>	0.030		

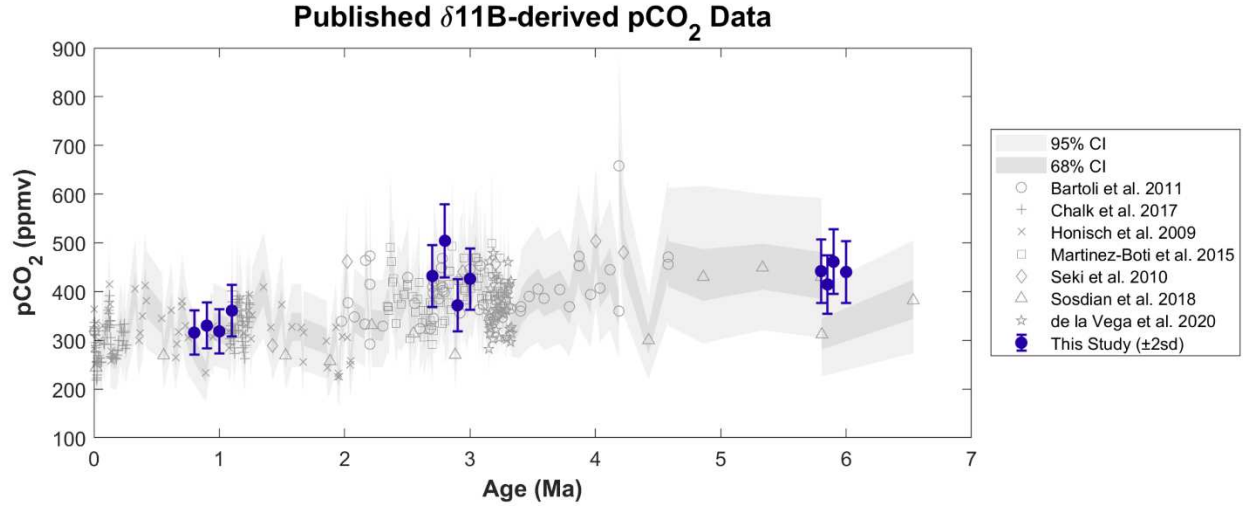


**Fig. S1.  $p\text{CO}_2$  from this study's pH compared to previously published  $\delta^{11}\text{B}$ -derived estimates of  $p\text{CO}_2$ .**

805  $p\text{CO}_2$  estimates (blue markers and error bars) made using pH proxy data of this study from the WEP, a region understood to be in equilibrium with the atmosphere<sup>25</sup>, assuming a modern-like alkalinity of 2275 mmol/kg. Error bars depict uncertainty ( $2\sigma$ ) returned from a Monte Carlo simulation ( $n = 10,000$  runs) including uncertainty from the pH estimate (i.e. uncertainty on measured  $\delta^{11}\text{B}$ , the  $\delta^{11}\text{B}$  composition of seawater<sup>42</sup>, SST, and sea surface salinity (SSS)), and  $\pm$

810 200 mmol/kg on alkalinity. Grey data points show  $\delta^{11}\text{B}$ -derived estimates of  $p\text{CO}_2$  from previously published studies, with shading showing reported confidence intervals<sup>43,62,82–86</sup>.

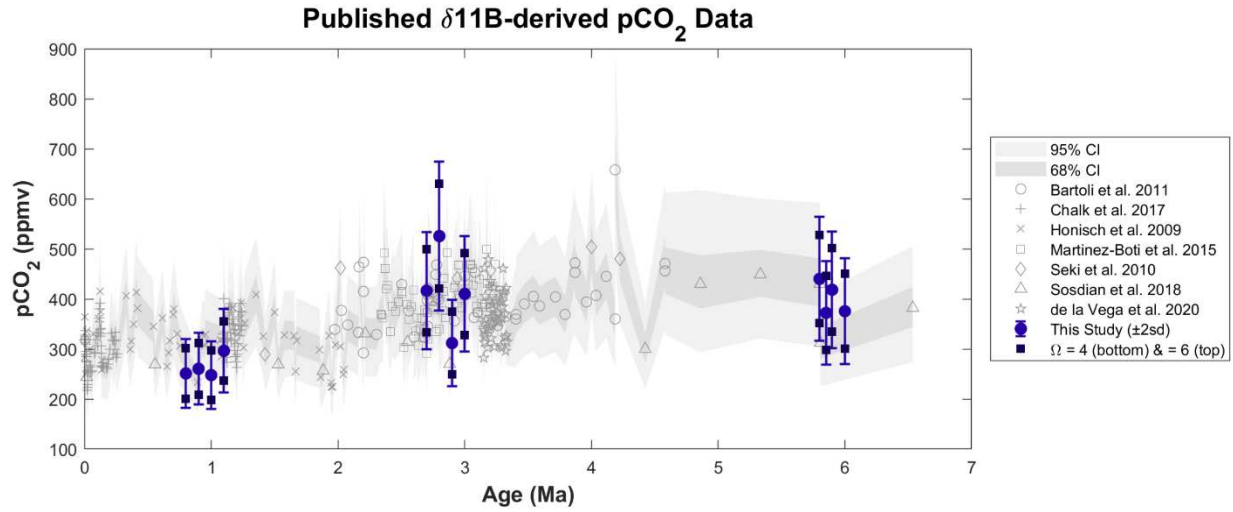


**Fig. S2.  $\text{pCO}_2$  from this study's pH assuming modern-like calcite saturation state.**

815 Same as Fig. S1 but assuming a modern-like calcite saturation state ( $\Omega = 5$ ). Error bars include a bracketing range of  $\pm 2$  on the value of  $\Omega$ . The black squares on each point show  $\text{pCO}_2$  when  $\Omega$  is not treated as a Monte Carlo variable and instead assigned an absolute value of 4 (lower  $\text{pCO}_2$  value) or 6 (upper  $\text{pCO}_2$  value), thus showing a plausible range of  $\text{pCO}_2$  for a  $\Omega$  range of 4-6.

820

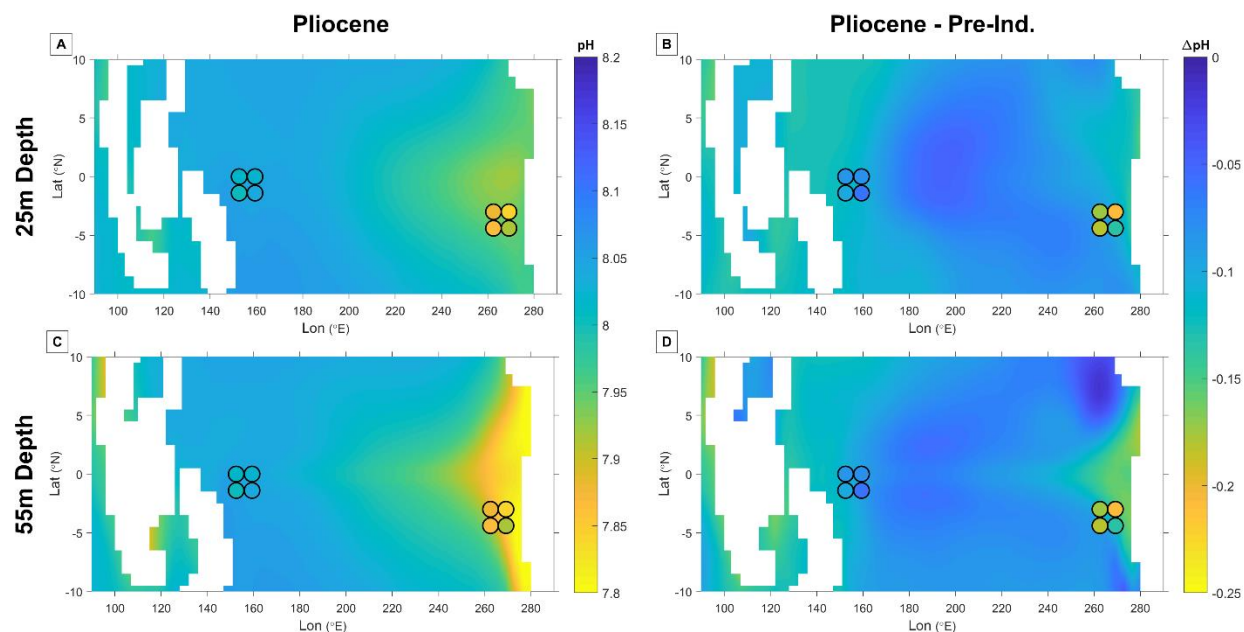


**Fig. S3. Model-data comparison of pH at 25m and 55m depth.**

Same as Fig. 3, but with 25m depth plotted (**A, B**) in addition to 55m depth (**C, D**).  $\delta^{11}\text{B}$ -derived pH values (colored squares) the same as in Figure 3, but the model output (colored contours) has been updated for 25m depth (**A, B**). (**A, C**) Climatological pH at 25m (**A**) and 55m (**C**) depth from the last 100 years of the 3000-year model run, interpreted to represent  $\sim 6\text{Ma}$  (colored contours), overlaid with  $\delta^{11}\text{B}$ -derived pH values (colored squares) of ages  $\sim 5.7$ ,  $\sim 5.8$ ,  $\sim 5.9$ , and  $\sim 6.0\text{Ma}$  starting with each location's top right square and going clockwise. More acidic waters are shown in yellow-green colors. (**B, D**) Same as (**A**) but depicting the difference in  $\sim 6\text{Ma}$  pH relative to pre-Industrial pH ( $\sim 6\text{Ma}$  minus Pre-Industrial, more acidic waters during the Pliocene shown in yellow-green colors) at 25m (**B**) and 55m (**D**) depth. Pre-Industrial pH derived from a pre-Industrial control run of the model for the contours and from Feely et al., 2009,<sup>31</sup> for the markers.

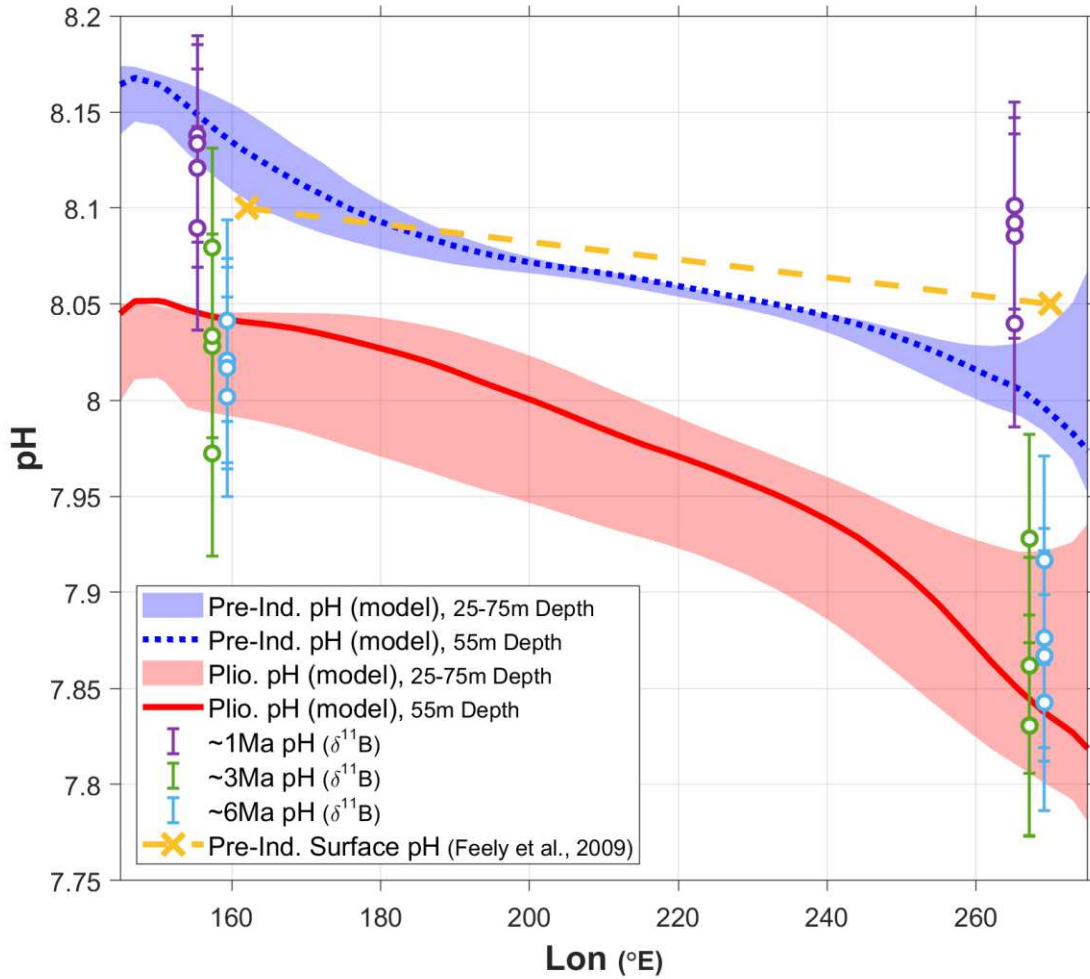
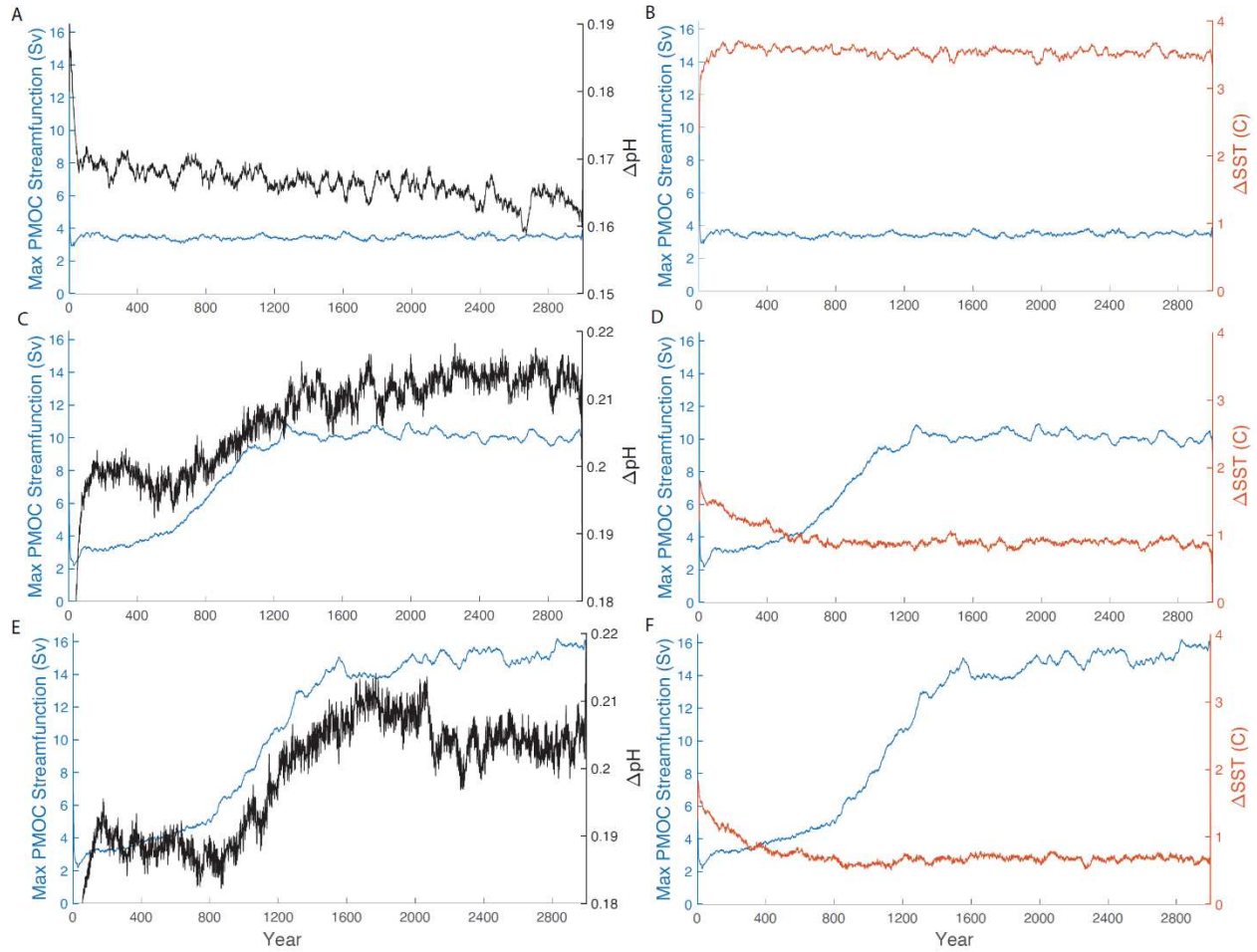


**Fig. S4. Longitudinal pH gradient in model and data.**

pH as derived from the model output (lines and shaded areas) and from  $\delta^{11}\text{B}$  measurements (circle markers, error bars show uncertainty ( $2\sigma$ ) returned by a Monte Carlo simulation, as in Figure 2B). Markers are placed at their approximate longitudes (latitudes are  $0^\circ\text{N}$  for western site ODP 806 and  $-3^\circ\text{N}$  for eastern site ODP 846). *O. universa* is understood to be a mixed-layer species<sup>36–38</sup> with a depth habitat ranging from  $\sim 0\text{--}75\text{m}$ , although it has been found at deeper depths<sup>87,88</sup>. The pre-Industrial longitudinal gradient in surface pH is included for reference<sup>31</sup>.



845 **Fig. S5. Timeseries of the strength of Pacific meridional overturning circulation (PMOC) and**  
**of zonal pH/SST gradients in model control and Pliocene runs.**

Timeseries plots showing strength of the PMOC (blue lines in all panels), the zonal Pacific pH  
gradient (“ $\Delta pH$ ”, black lines in panels A, C, and E), and the zonal Pacific SST gradient (“ $\Delta SST$ ”,  
red lines in panels B, D, and F) for **(A, B)** the model control run, **(C, D)** Experiment A, and **(E, F)**  
850 Experiment B. The strength of the PMOC (“Max PMOC Streamfunction”) is defined here as the  
maximum of the Pacific stream function north of 25°N and below 500m depth in Sverdrups (1 Sv  
=  $10^6 \text{ m}^3 \text{ s}^{-1}$ ). The pH gradient (“ $\Delta pH$ ”) is defined as the pH difference between a western Pacific  
box (5°S-5°N, 150-170°E) and an eastern Pacific box (5°S-5°N, 260-280°E), taken for values at

55m depth. The SST gradient (“ $\Delta$ SST”) is defined as the SST difference between the same boxes

855 (but for values taken at the surface instead of 55m depth).

860

865

870



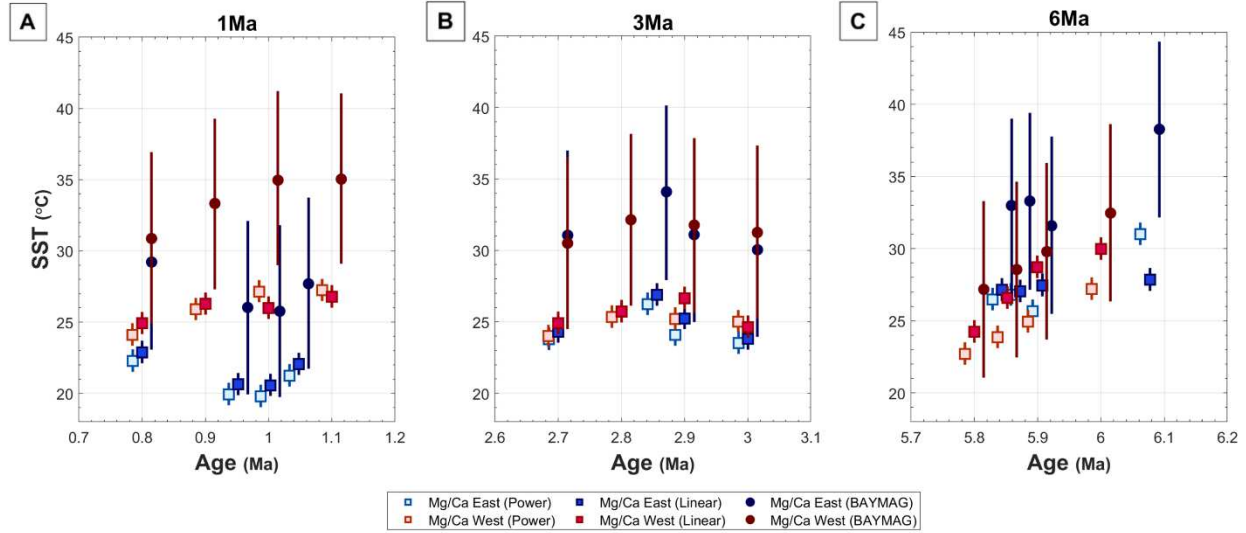


**Fig. S6. Mg/Ca SSTs derived from different calibrations and seawater corrections.**

Mg/Ca-derived sea surface temperatures (SSTs) for the eastern (site ODP 846, blue) and western (site ODP 806, red) equatorial Pacific at (A) ~1Ma, (B) ~3Ma, and (C) ~6Ma. Square markers show SSTs calculated from the *O. universa* SST calibration of Anand et al., 2003,<sup>68</sup> using a linear (dark square markers) and power-law (light square markers) relationship between  $Mg/Ca_{seawater}$  and  $Mg/Ca_{test}$ . Both use the  $Mg/Ca_{seawater}$  record of Fantle and DePaolo, 2006,<sup>59</sup>. For the power-law correction for  $Mg/Ca_{seawater}$ , because a coefficient of non-linearity has not yet been calibrated for *O. universa*, that of *T. sacculifer* ( $H = 0.41$ )<sup>89</sup> was used, following the example of previous boron-pH studies<sup>43</sup>. The same Mg/Ca was also calibrated into SSTs using the Bayesian calibration BAYMAG of Tierney et al., 2019,<sup>67</sup> and corrected for the Mg/Ca composition of seawater (circle markers). Error bars denote calibration errors on the linear- and power-corrected Mg/Ca SSTs (square markers) and 95% confidence intervals on the BAYMAG-calibrated data (circle markers). Note that only the data showing the linear correction for  $Mg/Ca_{seawater}$  (dark square markers) is plotted at the correct ages; the other two calibrations are offset to either side for ease of viewing.

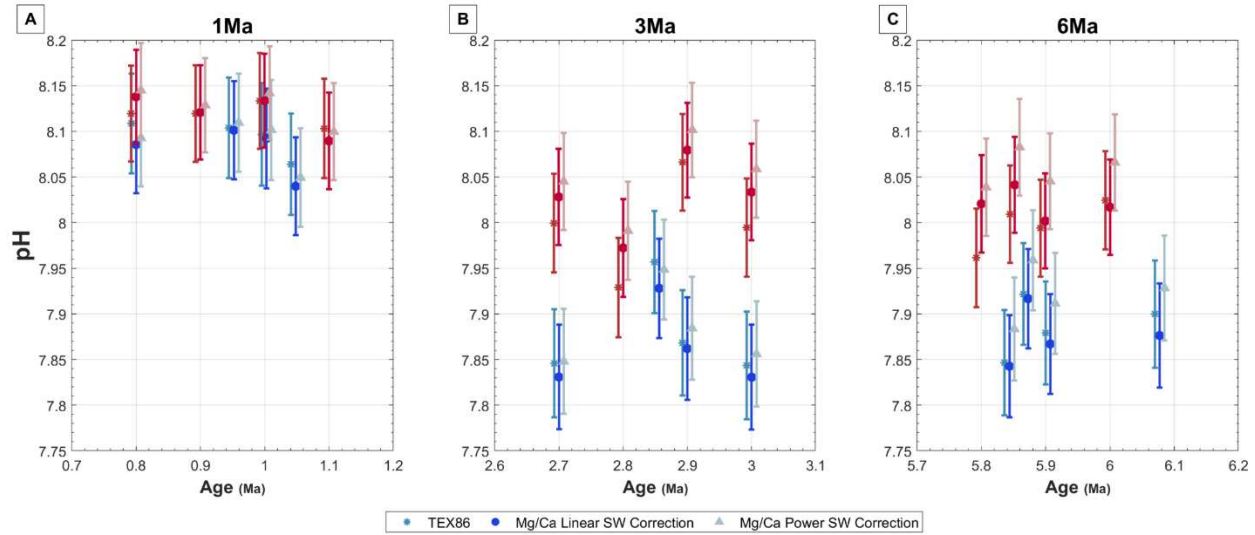


**Fig. S7. Calculated pH is largely insensitive to choice of SST proxy.**

pH derived from  $\delta^{11}\text{B}$  when calculated with three different records of SST at (A) ~1Ma, (B) ~3Ma, and (C) ~6Ma, in order to demonstrate the insensitivity of the boron-pH proxy to given temperature (SST) inputs. TEX86 SSTs derived from TEX86 data<sup>11</sup> from sites ODP 850 (east) and ODP 806 (west) using the calibration of Kim et al., 2010<sup>90</sup>. Mg/Ca SSTs were derived from Mg/Ca measurements made in this study, calibrated to SSTs using the *O. universa* calibration of Anand et al., 2003,<sup>68</sup>. Mg/Ca SSTs were corrected for the Mg/Ca composition of seawater ( $\text{Mg/Ca}_{\text{seawater}}$ ) in two different ways: assuming a linear relationship (circle markers) and a power-law relationship<sup>66</sup> (triangle markers) between  $\text{Mg/Ca}_{\text{seawater}}$  and  $\text{Mg/Ca}_{\text{test}}$ . Because a coefficient of non-linearity has not yet been calibrated for *O. universa*, that of *T. sacculifer*<sup>89</sup> ( $H = 0.41$ ) was used, following the example of previous boron-pH studies<sup>43</sup>. In both cases the  $\text{Mg/Ca}_{\text{seawater}}$  record of Fantle and DePaolo, 2006,<sup>59</sup> was used. All error bars depict uncertainty ( $2\sigma$ ) returned from a Monte Carlo simulation ( $n = 10,000$  runs) including uncertainty on  $\delta^{11}\text{B}$ , the  $\delta^{11}\text{B}$  composition of seawater<sup>42</sup>, SST, and sea surface salinity (SSS).

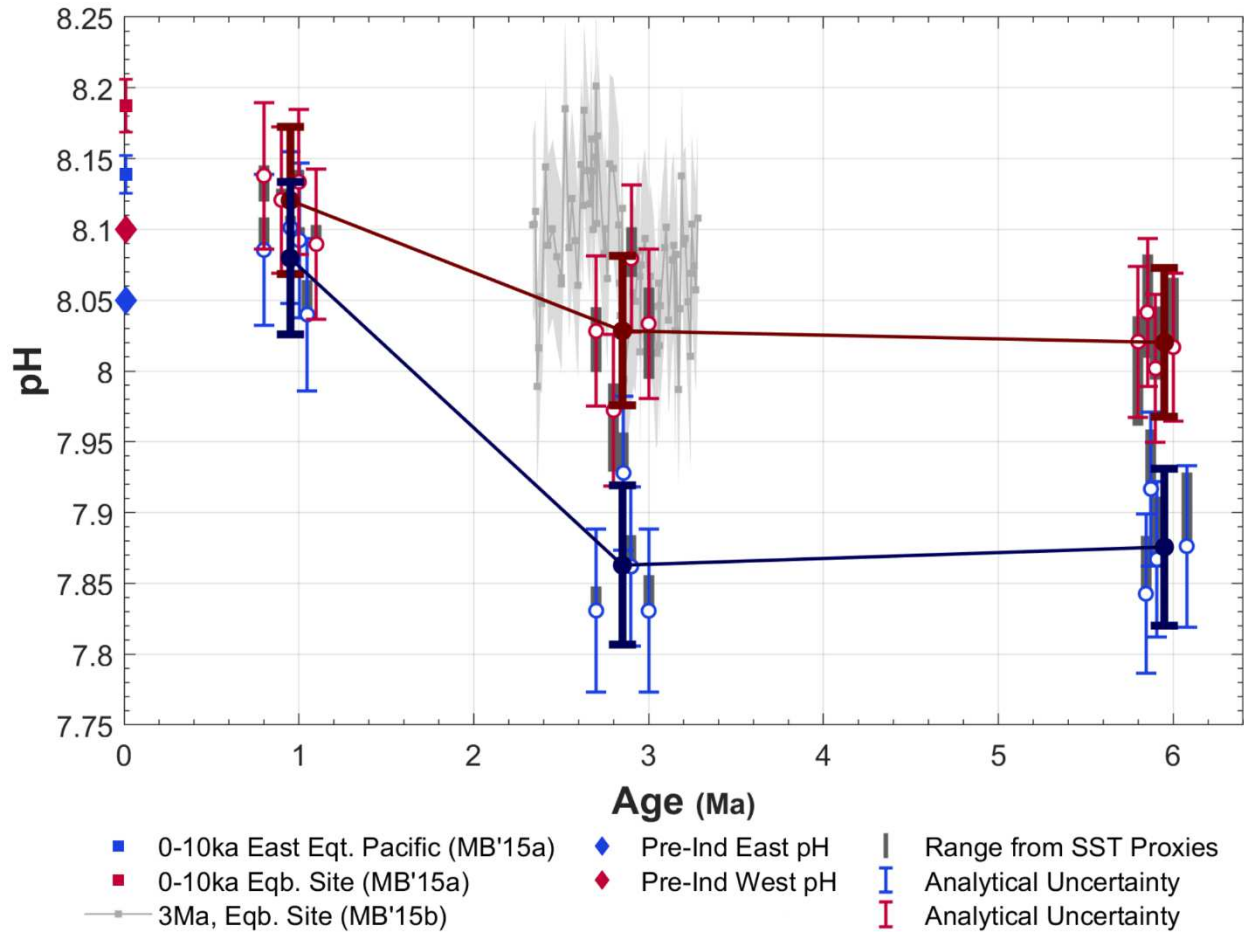


**Fig. S8. Western and Eastern Equatorial Pacific surface pH, 0-6Ma, from  $d^{11}B$  of planktonic foraminifera – showing range of different SST proxies used.**

Same as Fig. 2B but with the range of possible pH at each point from using different SST records in the pH calculation shown as superimposed dark grey bars. Range of possible pH at each point covers the range of pH estimates calculated using: TEX86-derived SSTs<sup>11</sup>, Mg/Ca-derived SSTs (this study) using a linear correction for  $Mg/Ca_{seawater}$ , and Mg/Ca-derived SSTs (this study) using a power-law correction<sup>66</sup> for  $Mg/Ca_{seawater}$ . Both Mg/Ca-SST calibrations were done using the  $Mg/Ca_{seawater}$  record of Fantle and DePaolo, 2006<sup>59</sup>.

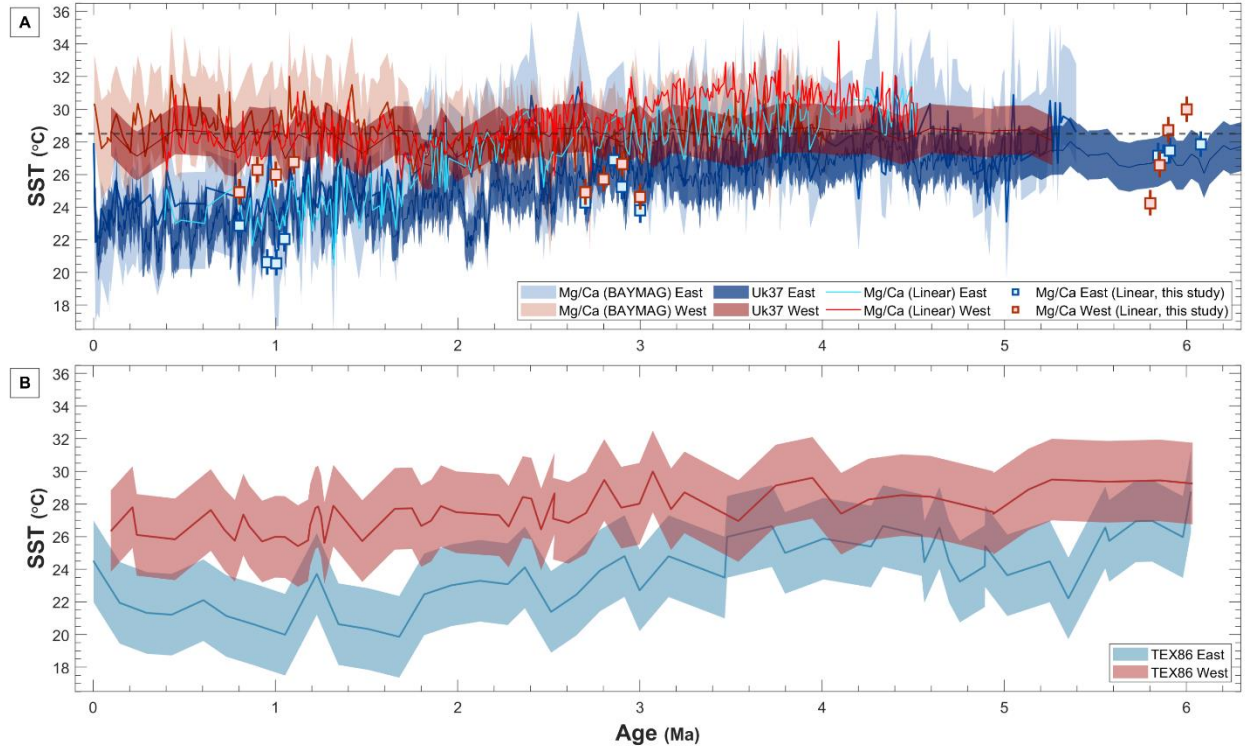


**Fig. S9. SST compilation, 0-6Ma.**

915 SST records from the eastern (blue) and western (red) equatorial Pacific. (A) SST records which  
 evince a collapse of the modern east-west SST gradient back into the Pliocene, derived from:  
 Mg/Ca data from *T. sacculifer* from sites ODP 847 (east) and ODP 806 (west) from Wara et al.,  
 2005,<sup>1</sup> calibrated using the Bayesian calibration BAYMAG<sup>67</sup> and corrected for the Mg/Ca  
 composition of seawater ( $Mg/Ca_{seawater}$ ) with 95% confidence intervals (pale blue and red bands);  
 920  $U^{K'}_{37}$  data from site ODP 846 (east)<sup>5</sup> and from site ODP 806 (west)<sup>11</sup> using the global ocean (60°N-  
 60°S) annual-mean calibration of Müller et al., 1998,<sup>91</sup> with its associated one standard error  
 ( $\pm 1.1^\circ\text{C}$ ) (dark blue and red bands) (dashed horizontal grey line shows the upper saturation of that  
 $U^{K'}_{37}$  proxy calibration); Mg/Ca data from *T. sacculifer* from sites ODP 847 (east) and ODP 806  
 (west) from Wara et al., 2005,<sup>1</sup> using the calibration of Dekens et al., 2002,<sup>92</sup> and corrected for  
 925  $Mg/Ca_{seawater}$  by O'Brien et al., 2014,<sup>9</sup> using the  $Mg/Ca_{seawater}$  record compiled in that study and  
 assuming a linear relationship between  $Mg/Ca_{seawater}$  and  $Mg/Ca_{test}$  (bright blue and red lines, no

uncertainty reported); and Mg/Ca data from *O. universa* from sites ODP 846 (east) and ODP 806 (west) compiled in this study using the species-specific calibration of Anand et al., 2003,<sup>68</sup> and corrected for Mg/Ca<sub>seawater</sub> using the Mg/Ca<sub>seawater</sub> record of Fantle and DePaolo, 2006,<sup>59</sup> assuming a linear relationship between Mg/Ca<sub>seawater</sub> and Mg/Ca<sub>test</sub> (square markers, with calibration error shown in error bars). **(B)** SST records which evince the modern east-west SST gradient being maintained back into the Pliocene, derived from TEX86 data<sup>11</sup> from sites ODP 850 (east) and ODP 806 (west) using the calibration of Kim et al., 2010,<sup>90</sup> with its associated calibration error ( $\pm 2.5^{\circ}\text{C}$ ) (blue and red bands).

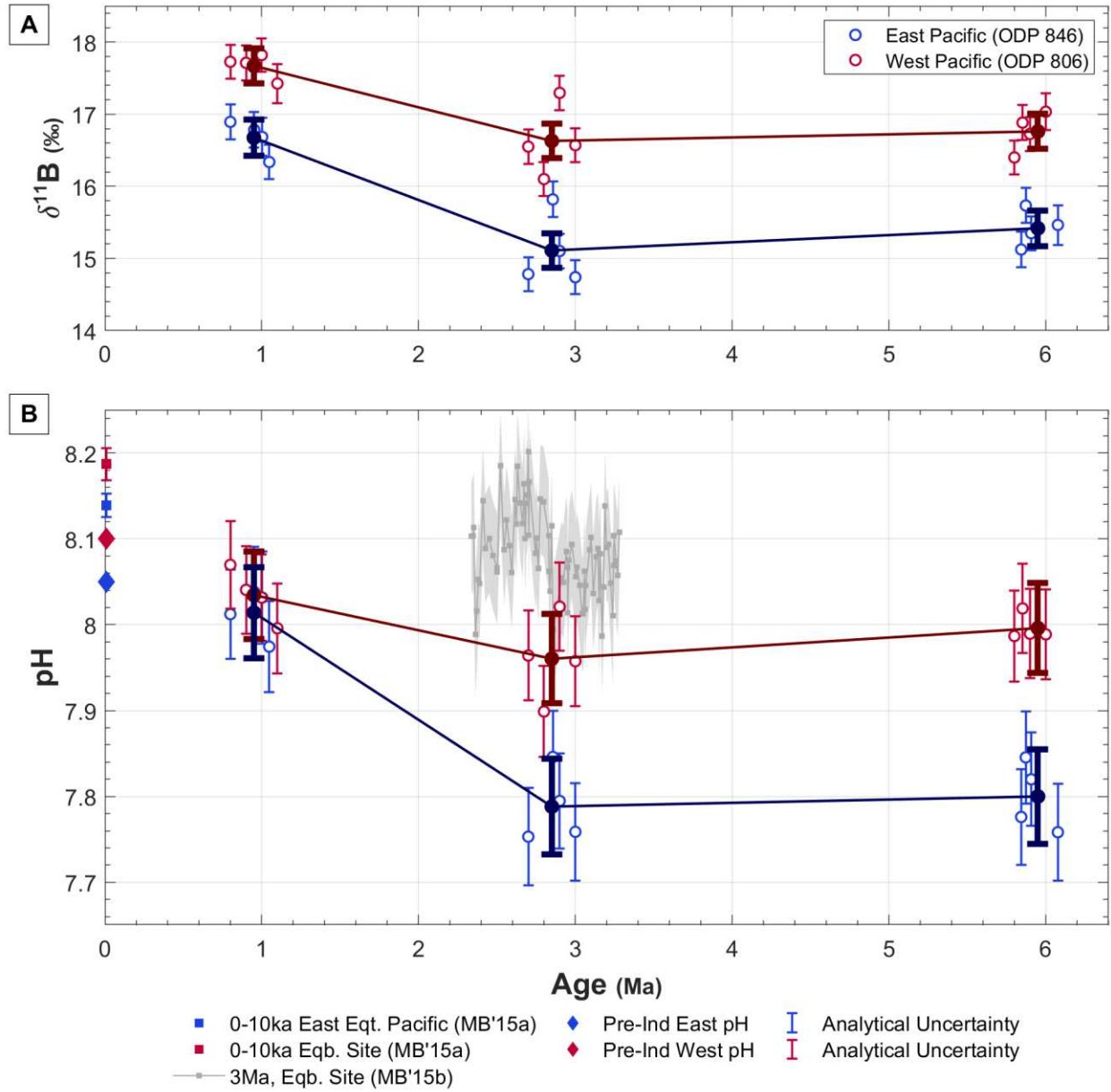


**Fig. S10. Western and Eastern Equatorial Pacific surface pH, 0-6Ma, from  $d^{11}\text{B}$  of planktonic foraminifera – using BAYMAG-calibrated Mg/Ca SSTs.**

Same as Figure 2, but with pH calculated using the SST record derived from calibrating this study's  
 940 Mg/Ca data with the BAYMAG calibration<sup>67</sup>. Note the change in y-axis (pH) scale on panel B  
 compared to Figure 2. (A) The boron isotopic composition ( $\delta^{11}\text{B}$ ) of *O. universa* from sites ODP  
 846 (east, blue) and ODP 806 (west, red). Analytical uncertainty ( $2\sigma$ ) included as error bars and

averages at ~1Ma, ~3Ma, and ~6Ma included as thickened, darkened points. **(B)**  $\delta^{11}\text{B}$ -derived pH  
for the same sites and time periods, in circle markers. Error bars depict uncertainty ( $2\sigma$ ) returned  
945 from a Monte Carlo simulation ( $n = 10,000$  runs) including uncertainty on  $\delta^{11}\text{B}$ , the  $\delta^{11}\text{B}$   
composition of seawater<sup>42</sup>, SST, and sea surface salinity (SSS).



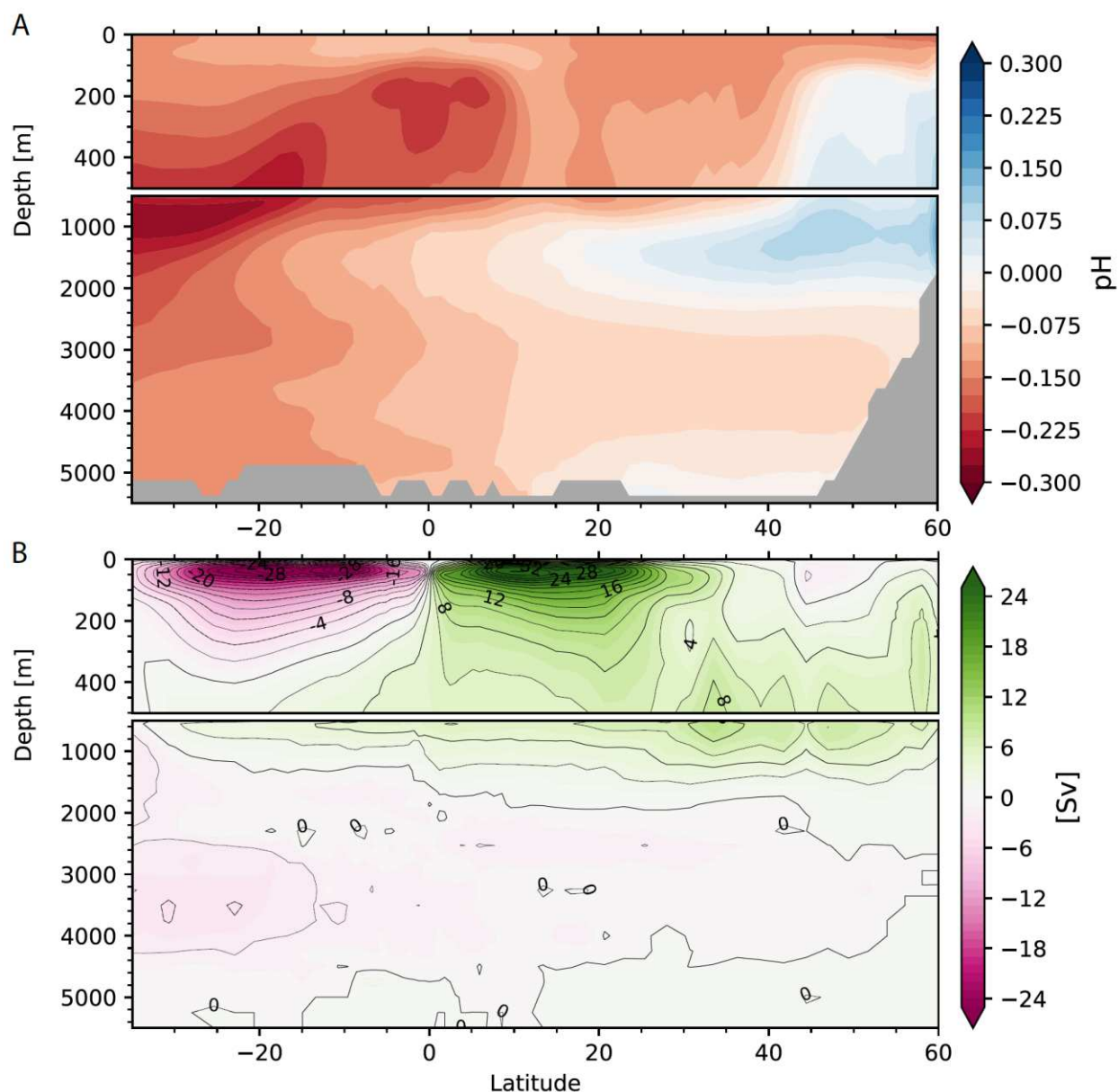


**Fig. S11. Interhemispheric pH and Water Mass Transport from Model Output – Experiment B.**

Same as Fig. 4 but for Experiment B (see Materials and Methods for description). **(A)** Zonally-averaged meridional transect of pH anomaly (Pliocene run minus preindustrial control run) and **(B)** zonally-averaged stream function.



## Figures

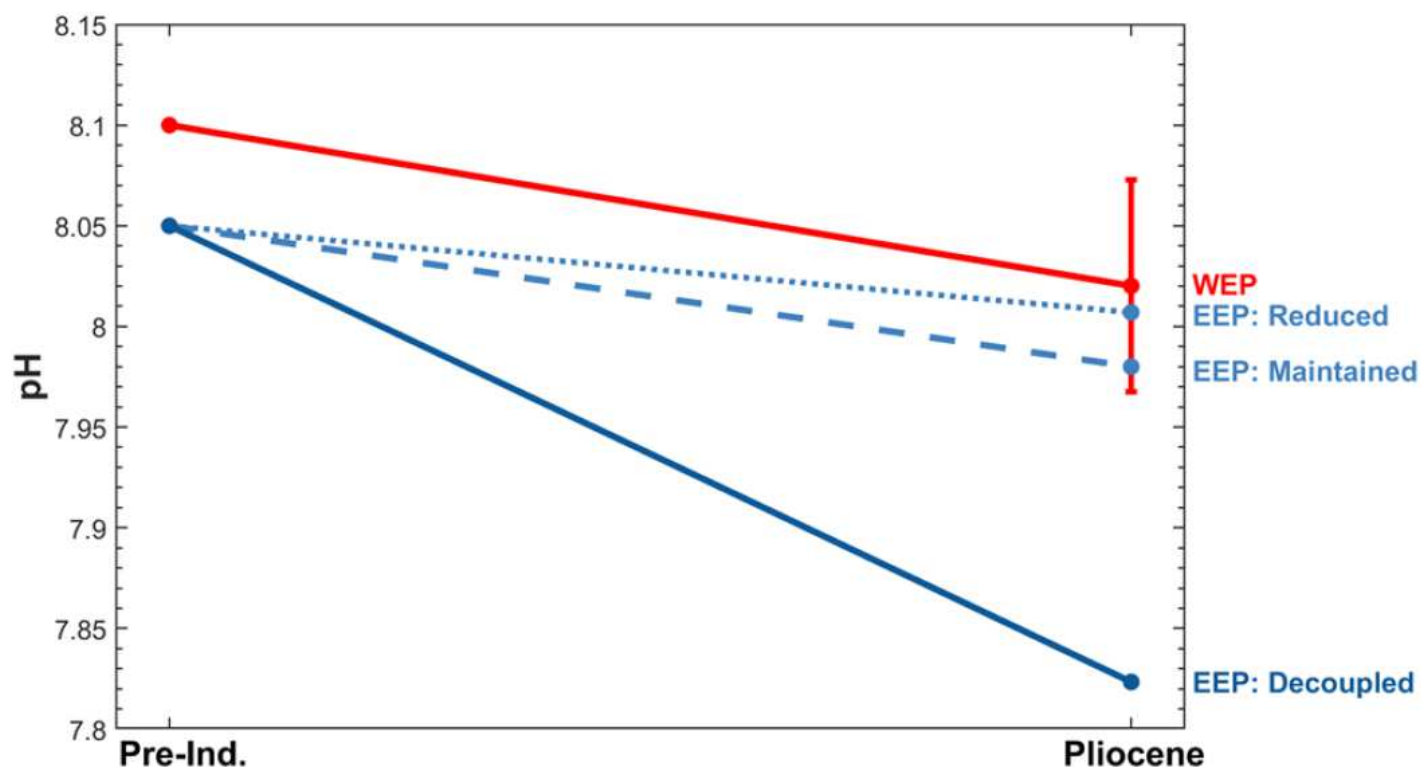


**Figure 1**

Alternative hypotheses for surface pH in the western and eastern equatorial Pacific, 0-6Ma. The strength of the east-west pH gradient is hypothesized to have been different in the Miocene/Pliocene than it is today, depending on dynamics dominating the climate system at that time. Red line: Pre-Industrial pH for the western equatorial Pacific (WEP) ( $\sim 8.1$ )<sup>31</sup> and pH from  $\sim 6$ Ma ( $\sim 8.02$ , the average  $\delta^{11}\text{B}$ -derived result of this study from  $\sim 6$ Ma at site ODP 806, with 2sd error bars). The blues represent three hypotheses for eastern equatorial Pacific (EEP) pH change relative to the pre-Industrial ( $\sim 8.05$ )<sup>31</sup>. Blue dotted line: coupled reduction in east-west temperature and pH gradients (i.e. same fractional change) during the Pliocene, with thermal gradient reduction as in Liu et al., 2019<sup>41</sup>. Blue dashed line: coupled reduction in Pliocene temperature and pH gradients (i.e. same fractional change), with a lesser reduction/maintained thermal gradient as in Zhang et al., 2014<sup>11</sup>. Blue solid line: decoupled changes in Pliocene temperature and pH gradients (i.e. pH gradient increased while thermal gradient reduced) as is predicted by the earth system model used in this study (output at 55m depth at location of site ODP 846 =  $\sim 7.82$ ).

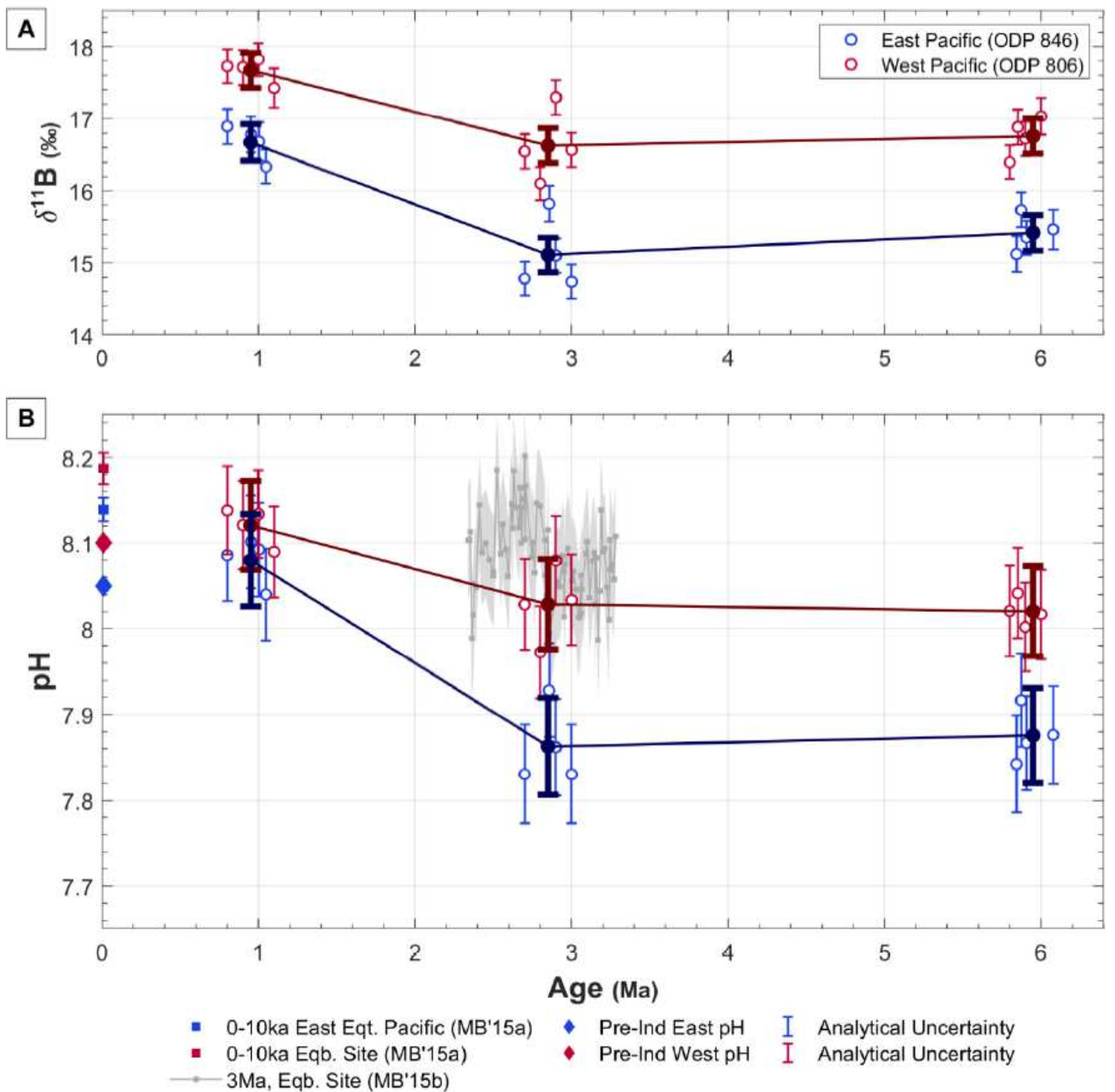


**Figure 2**

Western and Eastern Equatorial Pacific surface pH, 0-6Ma, from  $\delta^{11}\text{B}$  of planktonic foraminifera. (A) The boron isotopic composition ( $\delta^{11}\text{B}$ ) of *O. universa* from sites ODP 846 (east, blue) and ODP 806 (west, red). Analytical uncertainty [ $2\sigma$  included as error bars and averages at  $\sim 1\text{Ma}$ ,  $\sim 3\text{Ma}$ , and  $\sim 6\text{Ma}$  included as thickened, darkened points. (B)  $\delta^{11}\text{B}$ -derived pH for the same sites and time periods.  $2\sigma$  error bars produced by a Monte Carlo simulation ( $n = 10,000$  runs) including uncertainty on  $\delta^{11}\text{B}$ , the  $\delta^{11}\text{B}$  composition of seawater<sup>42</sup>, SST, and sea surface salinity (SSS). Additional pH data included for reference are: pre-Industrial estimates for the eastern and western Pacific (diamonds)<sup>31</sup>; average pH over

the last 10,000 years<sup>26</sup> from the eastern equatorial Pacific (blue square with 95% CIs, site ODP 1238) and from a site in equilibrium with the atmosphere (red square with 95% CIs, site PS 2498-1 in the southern Atlantic), and a mid-Pliocene ~3Ma equilibrium site<sup>43</sup> (grey points, ODP 999, central Caribbean with 95% CIs).

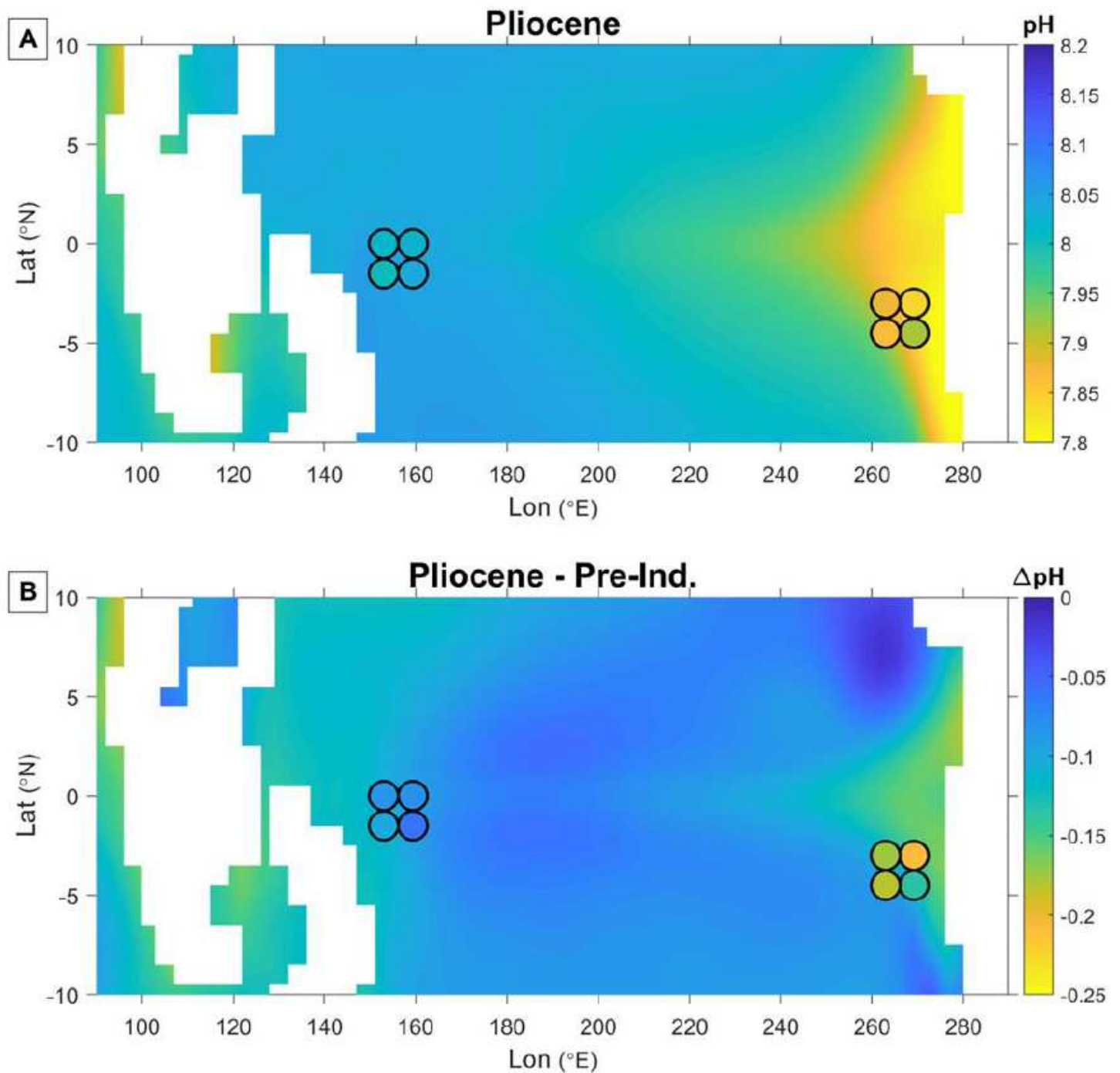


**Figure 3**

Model-Data comparison of pH at 55m depth. (A) Climatological pH at 55m depth from the last 100 years of the Pliocene simulation (colored contours), overlaid with  $\delta^{11}B$ -derived pH values (colored circles) of ages ~5.7, ~5.8, ~5.9, and ~6.0Ma clockwise from the top right. More acidic waters are shown in yellow-

green colors. (B) Same as (A) but depicting the difference in the Pliocene minus pre-Industrial control runs of the model (more acidic waters during the Pliocene shown in yellow-green colors). Colored circles show anomaly from the ~6.0Ma data to pre-Industrial pH from Feely et al., 200931.

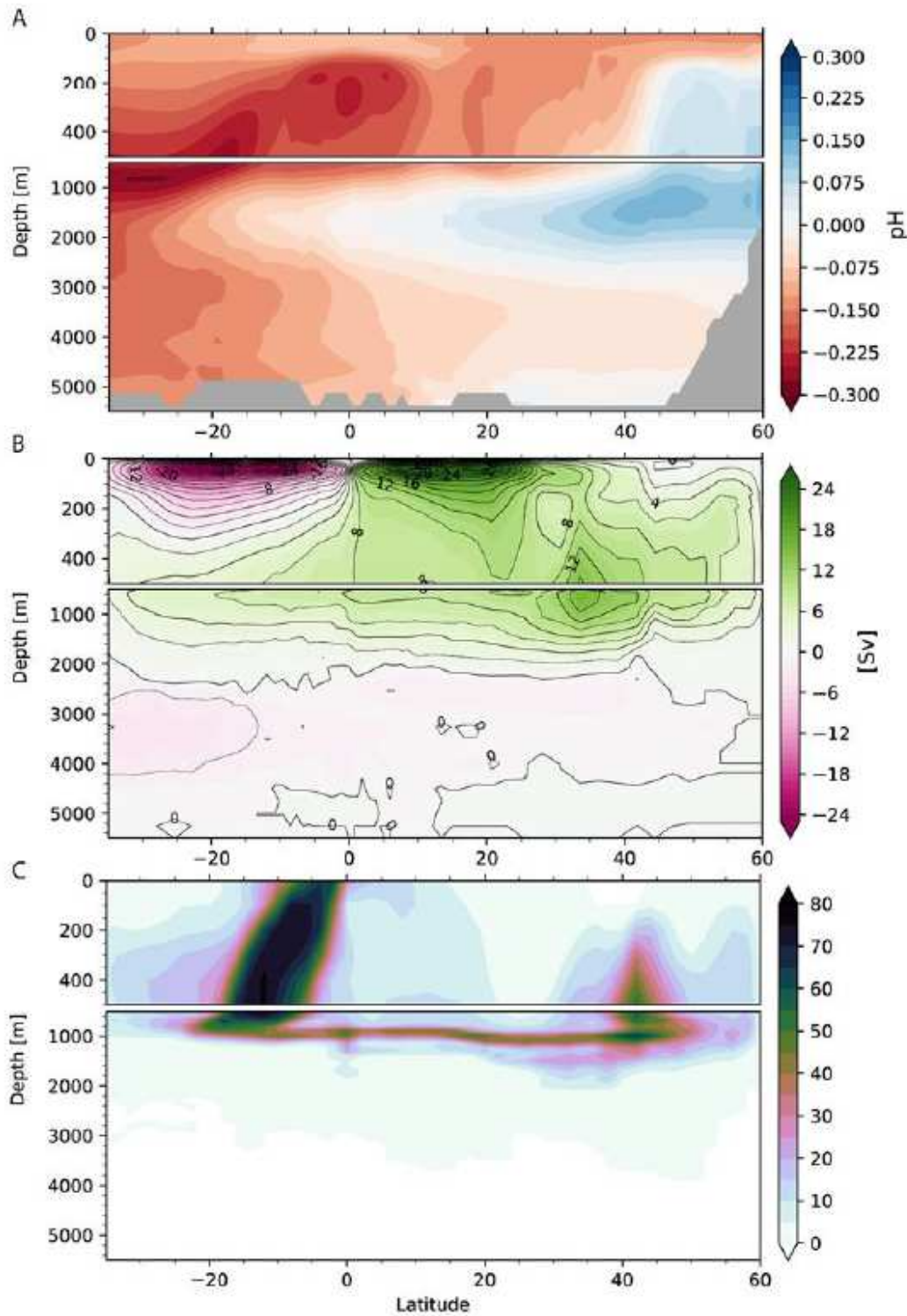


**Figure 4**

Model pH and water mass transport in the Pliocene Pacific. (A) Zonally-averaged meridional transect of the pH anomaly (Pliocene minus preindustrial control), (B) Pliocene zonally-averaged stream function,

and (C) latitude-depth pathways of water parcels sinking in the Pliocene subarctic North Pacific and upwelling in the tropical Pacific according to the Lagrangian analysis. Pathways are depicted as the percentage number of parcels that enter each model grid cell and, in effect, show the density of parcel trajectories that connect the northern Pacific deep-water formation regions with the tropical ocean (see Materials and Methods in the Supplement for details of the Lagrangian analysis).